Tiago Daniel Teixeira Gonçalves

Bachelor in Micro and Nanotechnologies Engineering

Implementation of X-ray reflectivity on the characterization of ultra-thin films for memory devices

Dissertation submitted in partial fulfillment
of the requirements for the degree of

Master of Science in
Micro and Nanotechnologies Engineering

Adviser: Joana Vaz Pinto, Assistant Professor,
Faculty of Sciences and Technology,
NOVA University of Lisbon

Co-adviser: Hugo Manuel Brito Águas, Associate Professor,
Faculty of Sciences and Technology,
NOVA University of Lisbon

Examination Committee

Chairperson: Rui Alberto Garção Barreira do Nascimento Igreja
Raporteurs: Luís Miguel Nunes Pereira
Joana Vaz Pinto

FACULDADE DE
CIÊNCIAS E TECNOLOGIA
UNIVERSIDADE NOVA DE LISBOA

September, 2018

Implementation of X-ray reflectivity on the characterization of ultra-thin films for memory devices

Copyright © Tiago Daniel Teixeira Gonçalves, Faculdade de Ciências e Tecnologia, Universidade NOVA de Lisboa.
A Faculty of Sciences and Technology e a NOVA University of Lisbon têm o direito, perpétuo e sem limites geográficos, de arquivar e publicar esta dissertação através de exemplares impressos reproduzidos em papel ou de forma digital, ou por qualquer outro meio conhecido ou que venha a ser inventado, e de a divulgar através de repositórios científicos e de admitir a sua cópia e distribuição com objetivos educacionais ou de investigação, não comerciais, desde que seja dado crédito ao autor e editor.

This document was created using the (pdf)LaTeX processor, based in the "novathesis" template[1], developed at the Dep. Informática of FCT-NOVA [2].
[1] https://github.com/joaomlourenco/novathesis [2] http://www.di.fct.unl.pt

Marco Polo describes a bridge, stone by stone.
"But which is the stone that supports the bridge?"Kublai Khan asks.
"The bridge is not supported by one stone or another,"Marco answers, "but by the line of the arch that they form."
Kublai Khan remains silent, reflecting. Then he adds:
"Why do you speak to me of the stones? It is only the arch that matters to me."
Polo answers: "Without stones there is no arch."
— Italo Calvino, *Invisible Cities*

Acknowledgements

Em primeiro lugar gostaria de agradecer à minha orientadora Prof. Dr. Joana Pinto. Agradeço por toda a disponibilidade que demonstrou, por todas as sugestões, pelo apoio e por ter sido a melhor orientadora que poderia ter tido.

Agradeço também ao Prof. Dr. Hugo Águas por ter sido meu coorientador e por toda a ajuda essencial com a elipsometria espetroscópica bem como pelas sugestões na organização da tese.

Ao Prof. Dr. Rodrigo Martins enquanto Presidente do Departamento de Ciências dos Materiais por todo o seu esforço e empenho que levou ao sucesso que hoje o MIEMN e o DCM se podem orgulhar de ter.

À Prof. Dr. Elvira Fortunato enquanto Diretora do CENIMAT pelo seu trabalho que não só resultou numa visibilidade internacional do CENIMAT mas também por ter tornado este centro de investigação excecional.

Ao Prof. Dr. Pedro Barquinha, à Eng. Cristina Fernandes, ao Eng. Jorge Martins, à Eng. Ana Rovisco, ao Prof. Dr. Jonas Deuermeier e à Prof. Dr. Asal Kiazadeh pela ajuda na recolha de amostras e dados fundamentais para esta tese.

À Dr. Sónia Pereira pela ajuda no esclarecimento de dúvidas sobre o difratómetro.

Ao Eng. Tomás Calmeiro pelas medidas de AFM bem como pela ajuda na análise das medidas.

À Sara Oliveira e à Sónia Soares pelo profissionalismo, simpatia e disponibilidade.

Por fim gostaria de agradecer à família, amigos e todas as pessoas que de alguma forma contribuíram para as boas memórias criadas ao longo destes 5 anos. Gostaria de agradecer em especial à Catarina Costa, ao Diogo Coelho (que também me ajudou na parte do inglês ao preço de 1 brownie/h), à Jaissica Vassantrai, à Joana Cerdeira, ao João Luís, à Leonor Matias, à Maria Leonor Abrunhosa, à Melissa Grandvaux, ao Miguel Ângelo, ao Miguel Pita, à Rita Cunha, à tia Rosalina Martins, à Prof. Ana Ávila Santos e ao Prof. Dr. Christopher Auretta. Muito obrigado.

Abstract

In this work X-ray reflectivity (XRR) was implemented as a characterization technique to study very thin films produced at CENIMAT. Three groups of samples were analysed: thin films of Ta_2O_5, thin films Ta_2O_5 mixed with SiO_2 (TaSiO) and thin films of zinc-tin oxide (ZTO). Spectroscopic ellipsometry was used as a complementary technique and all results were compared with the results of profilometry and Rutherford backscattering spectrometry (RBS).

A good agreement was found between the thicknesses obtained by all techniques. XRR revealed to be a better technique than SE to determine the thickness of the native oxide of silicon. In the same way the determination of the roughness was more accurate with XRR.

The objective of the characterization of the TaSiO and Ta_2O_5 samples was to study the influence of the radio frequency (rf) power in the Ta_2O_5 target during the sputtering process. In the case of the TaSiO samples an increase of the rf power resulted in an increase of the percentage of Ta_2O_5 and Ar in the films, as well as an increase of the density and dielectric constant. On the other side, the short-range order decreased. With the increase of the rf power the Ta_2O_5 samples only revealed a lower short-range order.

The aim of the characterization of the ZTO was to study of the effect of rf power in the ZTO target during the sputtering process, as well as the influence of the H_2 and O_2 flows. The increase of the rf power resulted in denser films with lower short-range order. In a less clear way a change in the H_2 influenced the films thickness. The increase of the O_2 flow had as a result films less dense and less rough.

Keywords: X-ray reflectivity, spectroscopic ellipsometry, thin films, Ta_2O_5, ZTO

Neste trabalho foi implementada a técnica de refletometria de raios-X (XRR) para a caracterização de filmes muito finos produzidos no CENIMAT. Três grupos de amostras foram analisadas: filmes finos de Ta_2O_5, filmes finos de Ta_2O_5 misturado com SiO_2 (TaSiO) e filmes de óxido de zinco e estanho (ZTO). Elipsometria espetroscópica (SE) foi utilizada como técnica complementar e os resultados foram comparados com os resultados de perfilometria e espectroscopia de retrodispersão de Rutherford (RBS).

Houve uma boa concordância entre as espessuras obtidas para todas as técnicas. XRR revelou ser uma melhor técnica do que SE para a determinação da espessura do óxido nativo das bolachas de silício. Da mesma forma, a determinação da rugosidade foi mais precisa com XRR.

O objetivo da caracterização das amostras de TaSiO e Ta_2O_5 era estudar a influência da potência de rádio frequência (rf) no alvo de Ta_2O_5 durante o processo de pulverização catódica. No caso das amostras de TaSiO o aumento da potência de rf resultou num aumento da percentagem de Ta_2O_5 e Ar nos filmes, assim como num aumento da densidade e da constante dielétrica. Por outro lado, a organização a curto alcance diminuiu. Com o aumento da potência de rf as amostras de Ta_2O_5 apenas revelaram uma diminuição da organização a curto alcance.

A caracterização das amostras de ZTO tinha como objetivo estudar o efeito da potência de rf no alvo de ZTO durante o processo de pulverização catódica, bem como a influência do fluxo de H_2 e de O_2. O aumento da potência de rf resultou em filmes mais densos e com menor organização a curto alcance. De forma menos clara a mudança do fluxo de H_2 influenciou as espessuras dos filmes. O aumento do fluxo de O_2 teve como resultado filmes menos densos e menos rugosos.

Palavras-chave: Refletometria de raios-X, elipsometria espectroscópica, filmes finos, Ta_2O_5, ZTO.

Contents

List of Figures xv

List of Tables xvii

Symbols xix

Acronyms xxi

Objectives xxiii

Motivation xxiii

1 Introduction 1
1.1 X-ray reflectivity 1
1.2 Spectroscopic ellipsometry 3
1.2.1 Theory 3
1.2.2 Tauc-Lorentz model 5
1.3 Ta_2O_5 films 5
1.4 ZTO films 6

2 Methods 7
2.1 Characterization techniques 7
2.2 Materials fabrication 8
2.2.1 Ta_2O_5 samples deposition process 8
2.2.2 Ta_2O_5/SiO_2 samples deposition process 8
2.2.3 ZTO samples deposition process 8

3 Results and discussion 9
3.1 Ta_2O_5 films 9
3.2 TaSiO samples 13
3.2.1 Growth rate determination (gr-TaSiO samples) 14
3.2.2 Dielectric layer (d-TaSiO samples) 19
3.3 ZTO samples 23
3.3.1 Influence of the rf power 25
3.3.2 Influence of the H_2 flow 26
3.3.3 Influence of the O_2 flow 27

4 Conclusions and future perspectives 29

Bibliography 31

A Abelès matrix formalism 37

B Tutorial of XRR data analysis in *MOTOFIT* 39

C Error functions of the performed fits **43**

D *Python* fuction to convert data to be used in *MOTOFIT* **45**

E Complementary schemes **47**

F Analysis of a silicon wafer **49**

G RBS analysis **51**

H Parameters of the Tauc-Lorentz models obtained by spectroscopic ellipsometry **53**

I The real and imaginary part of the dielectric function of the ZTO samples **57**

List of Figures

1.1 Data obtained by XRR of a tantalum pentoxide film on a silicon wafer. 1
1.2 Representation of the light interactions in a single layer system that leads to the creation of the Kiessing fringes. 2
1.3 Representation of the components of the electric field of a light beam [12]. . 3
1.4 Scheme of the spectroscopic ellipsometer used in this work (adapted from [12]). 4

3.1 Measured data by XRR and respective fits of Ta1 and Ta6 samples. 10
3.2 Comparison between the thicknesses obtained from XRR and SE. 11
3.3 Images of the surfaces of two samples obtained by AFM. 12
3.4 Real and imaginary part of the dielectric function obtained by SE. 12
3.5 Measured data and fit of the samples gr-Ta1Si and gr-Ta6Si. 14
3.6 RBS spectra from all samples with the respective fits in red. 15
3.7 Comparison between thicknesses obtained from XRR and SE. 17
3.8 Real and imaginary part of the dielectric function of the samples. 18
3.9 RBS spectra from all samples with the respective fits in red. 20
3.10 Real and imaginary part of the dielectric function of the samples. 21
3.11 Electrical measurements of the d-TaSiO samples. 22
3.12 Dielectric constants obtained from the electrical measurements. 23
3.13 Real data and XRR fit of the sample P1-O2-H1. 24
3.14 Comparison between thicknesses obtained from XRR and SE. 25

B.1 Reflectivity panel of *MOTOFIT* with the menu taps in the red boxes and the menu boxes in the green boxes. 39
B.2 An example of a model with fixed parameters. 40
B.3 Results of the SLD profile of the sample. 41
B.4 Results of the parameters of the sample with the respective uncertainties. . . 41
B.5 Results of the parameters of the sample with the respective uncertainties. . . 41

E.1 Model used to perform the fit of the data obtained by SE. 47
E.2 Scheme of the MIS structure. 47
E.3 Model used to perform the fit of the data obtained by SE to get the composition of the films. 47

F.1 Real data and XRR fit of the silicon wafer. 50

G.1 Fit and treated data measured by RBS from the gr-Ta5Si sample. 51

I.1 Real and imaginary part of the dielectric function of the samples characterized in section 3.3.1. 57
I.2 Real and imaginary part of the dielectric function of the samples characterized in section 3.3.2. 58
I.3 Real and imaginary part of the dielectric function of the samples characterized in section 3.3.3. 59

List of Tables

3.1 Nomenclature of the Ta_2O_5 samples. 9
3.2 Thicknesses obtained from Ta_2O_5 samples by XRR and SE using 20.0 Å as thickness in the SE data analysis. 10
3.3 The roughness obtained by XRR and AFM and the SLD obtained by XRR using Si and SiO_2 SLD values of 18.886×10^{-6} and 20.124×10^{-6} Å^{-2} respectively. . . 11
3.4 Nomenclature of both gr-TaSiO and d-TaSiO samples. 13
3.5 Results of the RBS fits. 15
3.6 Thicknesses obtained by profilometry, XRR, SE and RBS. 16
3.7 Calculated growth rates based on the obtained thicknesses. 16
3.8 Results from XRR and SE data analysis of the Ta_2O_5 and of the native oxide using Si and SiO_2 SLD values of 18.886×10^{-6} and 20.124×10^{-6} Å^{-2} respectively. 17
3.9 Thicknesses obtained by SE and RBS. 19
3.10 Composition in molecular % obtained by RBS and SE data analysis. 20
3.11 Thicknesses of the native oxide and roughnesses of the Ta_2O_5. 21
3.12 Samples nomenclature used in function of the fabrication parameters. 23
3.13 Results from XRR and SE data analyses of the samples with different target rf power using Si and SiO_2 SLD values of 18.886×10^{-6} and 20.124×10^{-6} Å^{-2}, respectively. 25
3.14 Results from XRR and SE data analyses of the samples with different H_2 flow using Si and SiO_2 SLD values of 18.886×10^{-6} and 20.124×10^{-6} Å^{-2}, respectively. 26
3.15 Results from XRR and SE data analyses of the samples with different O_2 flow using Si and SiO_2 SLD values of 18.886×10^{-6} and 20.124×10^{-6} Å^{-2}, respectively. 27

C.1 χ^2 of the fits performed in the Ta_2O_5 samples (section 3.1). 43
C.2 χ^2 of the fits performed in the TaSiO samples (section 3.2). 43
C.3 χ^2 of the fits performed in the ZTO samples (section 3.3). 43

F.1 Results of XRR and SE analyses of a silicon wafer using Si and SiO_2 SLD values of 18.886×10^{-6} and 20.124×10^{-6} Å^{-2}, respectively. 49

G.1 Results from the performed fit of the gr-Ta5Si sample. 51

H.1 Parameters from a Tauc-Lorentz oscillator of Ta_2O_5 samples (section 3.1). . . 53
H.2 Parameters from a double Tauc-Lorentz oscillator of TaSiO samples used to determine the grow rate (section 3.2.1). 53
H.3 Parameters from a double Tauc-Lorentz oscillator of TaSiO samples used as a dielectric material (section 3.2.2). 54
H.4 Parameters from a double Tauc-Lorentz oscillator of ZTO samples in the study of the influence of the rf power (section 3.3.1). 54

H.5 Parameters from a double Tauc-Lorentz oscillator of ZTO samples in the study of the influence of the H_2 flow (section 3.3.2). 55
H.6 Parameters from a double Tauc-Lorentz oscillator of ZTO samples in the study of the influence of the O_2 flow (section 3.3.3). 55

Symbols

Δ	Change in the polarization of the light after the interaction with the material.
ψ	Change in the amplitude of the components of the electric field after the interaction with the material.
λ	Wavelength.
θ	Angle.
χ^2	Error function.
ε_∞	High frequency dielectric constant.
ε_1	Real part of the dielectric function.
ε_2	Imaginary part of the dielectric function.
α_c	Critical angle.
$\sigma_{n,n+1}$	Roughness or diffusenes of a layer.
A	Transition matrix element.
C	Broadening term.
E	Photon energy.
E_0	Peak transition energy.
E_g	Band gap energy.
Q	Momentum transfer.
d_K	Distance between two peaks of the Kiessing fringes.
k_z	Wave factor.
r_p	Amplitude reflection coefficients of the incident parallel polarized wave.
r_s	Amplitude reflection coefficients of the incident perpendicularly polarized wave.

Acronyms

AFM	Atomic Force Microscopy.
CENIMAT	Materials Research Center.
DRAM	Dynamic Random Access Memory.
GIZO	Indium-Gallium-Zinc Oxide.
MIS	Metal-Insulator-Semiconductor.
RBS	Rutherford Backscattering Spectrometry.
rf	radio frequency.
RRAM	Resistive Random Access Memory.
SE	Spectroscopic Ellipsometry.
SLD	Scattering Length Density.
TaSiO	mixture of Ta_2O_5 and SiO_2.
TFT	Thin-Film Transistor.
XRR	X-ray Reflectivity.
ZTO	Zinc-Tin Oxide.

Objectives

Nowadays the memory devices are based on thin films that are becoming even thinner. However the development of thinner films leads to a problem: the characterization of those films. With thicknesses that can be lower than 10 nm, the implementation of techniques capable of measure such thicknesses are crucial in order to continue the scientific research in the field of memory devices.

Taking that in mind the main objective of this work was the implementation of X-ray Reflectivity (XRR) to characterize thin and ultra-thin films at Materials Research Center (CENIMAT). Some of the XRR experiments were performed before the beginning of the thesis but due to the lack of a data analysis method, the determination of the properties of the films was not possible. The implementation of such method turned possible the use of XRR at CENIMAT. By using spectroscopic ellipsometry (SE) one aimed to confirm the success of the XRR data analysis method as well as study the limitations and information one can get from both techniques.

To test the analysis method, some sets of samples of the research group were analysed. Films of Ta_2O_5 mixed with SiO_2, Ta_2O_5 and zinc-tin oxide (ZTO) were used. The variation of the used radio frequency power in the target during the sputtering process was studied in all samples. In the ZTO samples the variation of the H_2 and O_2 was also studied.

Motivation

One must do everything that is possible with the available resources. That was the spirit behind this work. CENIMAT has a diffractometer that enables XRR characterization. The implementation of a protocol to analyse the XRR measured data would turn possible the use of the diffractometer for another characterization technique (besides X-ray Diffraction) with no additional costs.

Besides that, until the beginning of this thesis the characterization of some thin films produced at CENIMAT had been a challenge. Semiconductor films for thin-film transistors with thicknesses between 20 and 40 nm, dielectric and semiconductor films produced by solution process and storage layers in memory devices below 10 nm are some examples where other characterization techniques can not be successfully used.

In order to fill the need of using a technique that could be useful in the characterization of such films and by taking advantage of the possibility that XRR data can be obtained at CENIMAT, the implementation of a method to analyse XRR data was crucial. Using SE that already was a very well established technique at CENIMAT, it was possible to complement the XRR characterization with SE. So, a more complete characterization of the samples was achieved.

Introduction

1.1 X-ray reflectivity

Nanostructured devices are becoming more used in many fields like microelectronics, optoelectronics and sensors. These devices use thin films that are becoming thinner with the evolution of fabrication processes. With this reduction of thickness and with the use of multilayers films, some physical properties of the films and their interfaces become crucial for the correct function of the devices [1].

X-ray Reflectivity (XRR) is a non-destructive method of characterization that can analyse crystalline and amorphous single and multilayer thin films. This technique takes advantage of the fact that matter has a refractive index for X-rays smaller than one. As a result, for angles below a specific critical angle, the incident X-rays are reflected. In other words, occurs a total external refraction. This physical property makes it possible to get information about the material density. Besides that, with this technique it is possible to obtain the film thickness (precision below 1 nm) and the roughness of the surface and interfaces [1, 2].

The critical angle (α_c) can easily be obtained from the angle from which the measured intensity drops rapidly. After being obtained, the critical angle can be used for a density analysis. The thickness of a film can also be easily obtained and this parameter is related to the angular distance between oscillation waves in the intensity of reflected light - Kiessing fringes (d_K) [1]. As an example, a XRR curve is plotted in Figure 1.1 illustrating the determination of the α_c and d_K.

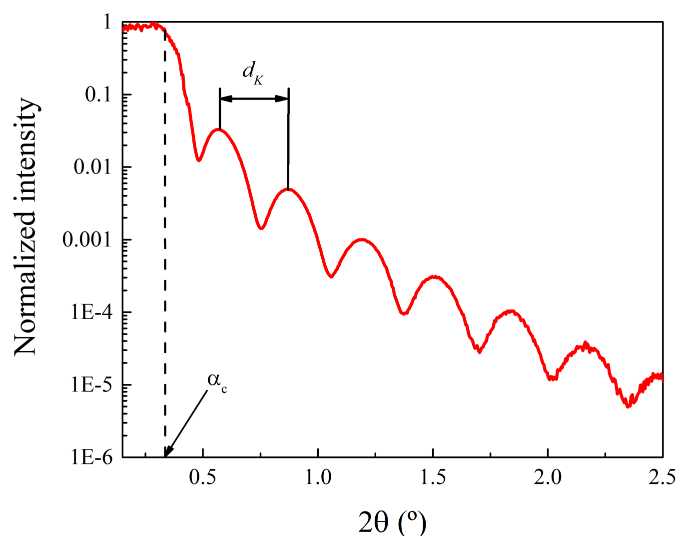

Figure 1.1: Data obtained by XRR of a tantalum pentoxide film on a silicon wafer.

The Kiessing fringes are due to the constructive and destructive interactions between the reflected waves. An explanation of this interactions is represented in Figure 1.2. In this figure one takes as an example a sample with a single film. Part of the incident beam

is reflected and other the part penetrates the film. The part of the beam that penetrates the film will be divided again: part will be reflected in the interface between medium 2 and 3 and part will penetrate the medium 3 and so on. All the components of the initial incident beam that will go out to medium 1 will interact with each other [3]. Here it is considered just the specular part of the beam (when the angle of the incident beam is equal to the angle of the reflected beam) [1].

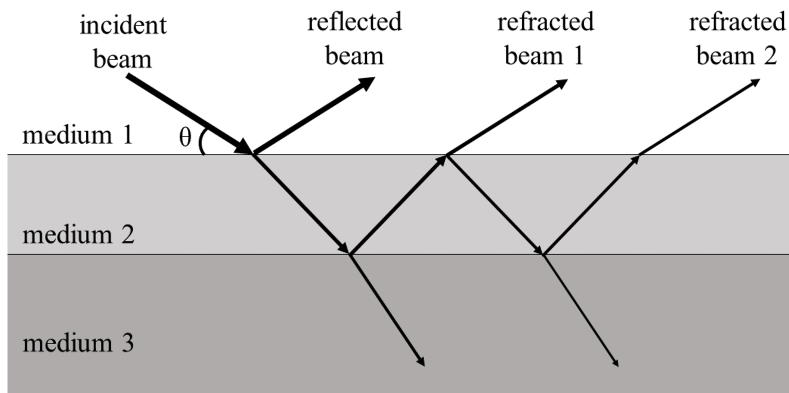

Figure 1.2: Representation of the light interactions in a single layer system that leads to the creation of the Kiessing fringes.

It is usual to use mathematical formalism to analyse the measured data. In this work the analyses of XRR data were performed in the *MOTOFIT* package [4]. This package uses the Abelès matrix formalism [5]. In Appendix A is possible to find more information this formalism.

There are a few set-ups that can be used to perform XRR analyses. In the set-up used in this work both the X-ray source and the detector moved and the sample is kept fixed. The other possibility in rotate the sample at the same time as the source moves. In this case the detector is fixed. Nevertheless, in these two set-ups the angle between the source-sample and sample-detector is the same, as one only uses the specular part of the reflected beam [1, 2].

Despite same differences, in all set-ups a high intense X-ray source and a low noise detector is necessary. This is due the fact that the range of orders of magnitude of the measure intensity can be higher than 5. In the example shown in Figure 1.1 the range of the measured intensity has almost 6 orders of magnitude. Not only that but the alignment of the sample is crucial and should be performed carefully [1, 2].

In this thesis XRR was used only to know thicknesses, roughnesses and Scattering Length Density (SLD) (a parameter proportional to the mass density) in a dry medium. Despite that, XRR has been used in more applications. For example, XRR can be used to study layers in a liquid medium [6] as well as liquid-liquid and air-liquid interfaces [7], to do image reconstruction of the samples [8], to determine the element depth profiles in low contrast multilayers systems [9], to determine the electron density profile of a electrolyte solution inside nanotubes [10] or even to calibrate ellipsometers [11].

1.2 Spectroscopic ellipsometry

1.2.1 Theory

Ellipsometry is a non-destructive optical characterization technique that characterizes light that is reflected from a sample. It can also characterize transmitted light, but this work focuses only on the reflection mode. It measures the change that occurs in the polarization of light with the interaction light-material. This technique is named «ellipsometry» because, with this interaction, linearly polarized light usually becomes «elliptical» [12].

Light is an electromagnetic wave composed by an electric field and a magnetic induction which are perpendicular to each other. The electric field is used to describe the polarization state of light. For that, when a light beam is travelling along the z axis, its associated electric field can be decomposed in two components: one parallel to the x axis and another parallel to the y axis (Figure 1.3a). These components are described by the propagation number (that depends on the wavelength), their initial magnitude and initial phase [12].

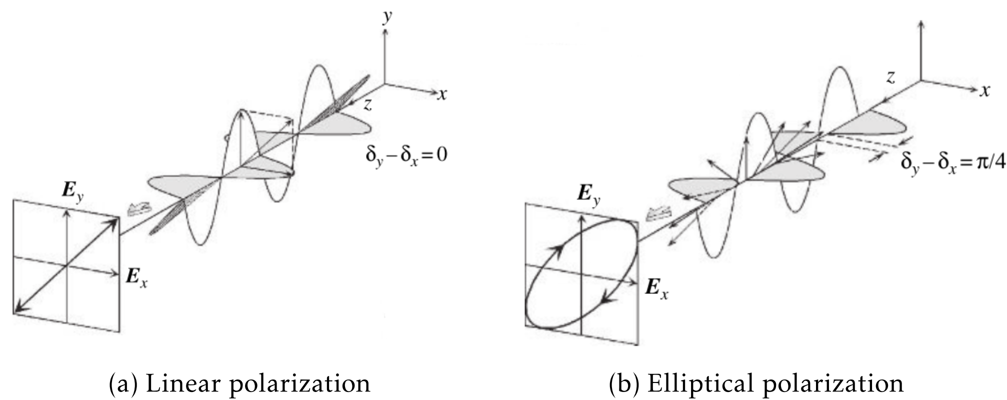

(a) Linear polarization (b) Elliptical polarization

Figure 1.3: Representation of the components of the electric field of a light beam [12].

The polarization state is directly correlated with the difference between the two components, in the amplitude and in phase. When there is no difference in the initial phases the result is an electromagnetic wave with planar polarization state. When this difference is not zero, the synthesized vector rotates with the propagation of light, which results in an elliptical polarization (Figure 1.3b). The particular case when the difference is equal to $\pi/2$ the polarization state is circular [12].

With the interaction with matter, the phase of the electric field can change and this change depends on the refraction index. Because of that, one of the values measured in ellipsometry to characterize the sample is the change in the polarization of the light, witch is represented by Δ [12].

Besides the change in phase, the amplitude of the components of the electric field can also change with the reflection. The change is represented by ψ, that is defined by:

$$tg(\psi) = \frac{r_p}{r_s} \tag{1.1}$$

where r_p and r_s are the amplitude reflection coefficients of the incident parallel polarized wave (r_p) and the perpendicularly polarized wave (r_s) to the plane of incidence. These coefficients are given by Fresnel equations [12].

These two values (ψ, Δ) express the change in phase and amplitude that appends in light with the reflection on the sample. So, in ellipsometry, the change in the emitted light is measured as the change in the polarization state and this is represented by the fundamental equation of ellipsometry [12]:

$$\rho = tg(\psi)exp(i\Delta) \tag{1.2}$$

If one takes as an example a simple structure, ψ characterize the refractive index of the sample and Δ describes the extinction coefficient. Therefore, these two values measured by Spectroscopic Ellipsometry (SE) describe directly two properties of the sample. This example represents the basic principle of elipsometry [12].

Until here, it has been described the ellipsometry technique, however in this work it was used SE that has the same fundaments of the ellipsometry but uses a light spectra instead of a monochromatic light. Using SE today it is possible to determine many physical properties of the sample with the two values measured (ψ, Δ) as function of the wavelength or energy, namely the complex refractive index, complex dielectric function, absorption coefficient, film thickness, band gap and free-carrier absorption. To obtain these properties, it is necessary to create optical models to analyse the SE data. For the creation of those models, it is crucial to have as much information as possible of the sample, like approximate thicknesses and materials [12].

A spectroscopic ellipsometer is required to do SE analyses. In the system used in this thesis, the light ray comes from a polychromatic light source, passes through a linear polarizer and then the sample is subjected to this incident light. After the reflection, light (now elliptical polarized) passes through a periodic modulator and an analyser. Finally, light reaches the detector that measures the intensity of light [12]. A scheme of this system can be found in the figure below.

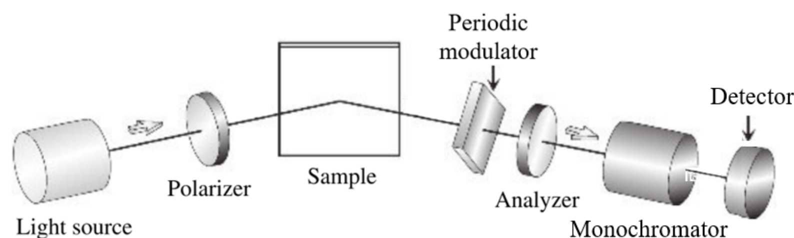

Figure 1.4: Scheme of the spectroscopic ellipsometer used in this work (adapted from [12]).

1.2.2 Tauc-Lorentz model

In order to analyse the experimental data, one needs a mathematical function. One of the most well-known is the Tauc-Lorentz dispersion formula [13]. This formula is the junction of the Tauc joint density states [14] and the Lorentz calculation of the imaginary part of the dielectric function (ε_2) [15]. This is given by [13]:

$$\varepsilon_2(E) = \begin{cases} \dfrac{AE_0C(E-E_0)^2}{\left(E^2-E_0^2\right)+C^2E^2}\dfrac{1}{E}, & E > E_g \\ 0, & E \leq E_g \end{cases} \tag{1.3}$$

where A is the transition matrix element, C is the broadening term, E is the photon energy, E_0 is the peak transition energy and E_g is band gap. All these parameters are in energy units and, except E, are fitting parameters. E is the variable and the fitting is performed as function of E.

Doing a Kramers–Kronig integration of the equation 1.3 it is possible to obtain the real part of the dielectric function. With this integration a new fitting parameter appears, ε_∞, which represents the high frequency dielectric constant [13].

1.3 Ta_2O_5 films

Given the decrease of devices dimensions, it is important to find materials with high dielectric constant to be an alternative to SiO_2 [16–18]. One of the most studied materials is the Ta_2O_5 that has a high dielectric constant, high refractive index [19, 20] and has been studied using both XRR [21–23] and SE [17, 24–27]. Due to its properties, Ta_2O_5 has been used in several applications such as Dynamic Random Access Memory (DRAM) [19, 28] and redox-based Resistive Random Access Memory (RRAM) [29].

Taking into account the number and diversity of applications, it is crucial to understand the relation between the fabrication methods and the film's properties. For example, a change in the dielectric constant of Ta_2O_5 with variations in the deposition process has already been reported [30, 31]. Furthermore, for the Ta_2O_5 application as redox-based RRAM has been shown that the change in the film density can affect the device behaviour [32].

In order to improve the properties of Ta_2O_5 films to be used as dielectric layer in transistors, a mixture of Ta_2O_5 and SiO_2 (TaSiO) can be used. TaSiO film presents a lower leakage current, a lower hysteresis magnitude and a faster recovery of the threshold voltage, compared to a Ta_2O_5 film. Besides that, the use of a substract bias can even lower the leakage current. So, using a mixture with SiO_2 and substract bias, one can have thinner films and with better properties [24, 33].

In this work TaSiO films were produced by radio frequency (rf) co-sputtering with subtract bias. The objective was to study the influence of the rf power in the Ta_2O_5 target in the thickness, density and roughness of the films. After that, a study of the same

nature was performed in Ta_2O_5 films, also produced by rf sputtering with subtract bias. The fabrication conditions were the same for both studies to be possible to compare the results.

1.4 ZTO films

Thin-Film Transistor (TFT) is a device with many applications such as displays and solar cells. In order to have a better performance of TFTs for this application, amorphous oxide semiconductor has been studied to substitute technologies like a-Si:H TFTs. This is due to the excellent uniformity in large areas, high transparency and good electric performance [34–36].

Indium-Gallium-Zinc Oxide (GIZO) is one of the amorphous oxide semiconductors used. This material presents a good electrical performance in displays and solar cells and can be fabricated at room temperature [35]. However, according to a report published in January 2018 by the European Commission [37], both indium and gallium are in the list of critical raw materials and have an end-of-life recycling input rate close to 0 %. So, indium- and gallium-free TFTs have been studied.

Zinc-Tin Oxide (ZTO) has been widely studied as an alternative to GIZO due to its performance and the fact that it does not use critical raw materials. It presents many advantages such as being cheap, non-toxic, having good physical robustness, film smoothness, chemical stability and good transparency [38–42]. Recently was shown that ZTO can be used to fabricate flexible TFTs at low temperature. Not only that but it was also demonstrated that the electric performance of the TFTs is improved with the incorporation of hydrogen in the ZTO layer [34].

In the present work ZTO films were produced using different parameters. With this approach one aimed to study the influence of parameters like H_2 and O_2 flow during the rf sputtering fabrication in the density, roughness and thickness of the films.

Chapter 2

Methods

2.1 Characterization techniques

XRR was performed using the PANalytical's X'Pert PRO MRD X-ray diffractometer with a monochromatic source of CuKα (λ = 1.540 598 Å). To perform a XRR analysis both the X-ray source and detector move, changing the angle (θ) relatively to the sample. The 2θ scan range used in this work was from 0.1000° to 4.0000° with a step size of 0.0050°. With this analysis one can take the thickness, roughness and SLD for each film. The data analysis was done in the *MOTOFIT 4.1* package [4]. A tutorial of the data analysis can be found in Appendix B and all error functions of the performed fits in the Appendix C.

However, the files obtained by XRR cannot be directly used in *MOTOFIT 4.1*. As an output, the diffractometer gives the angle (2θ) and the respective measured intensity. As an input, *MOTOFIT 4.1* needs the photon momentum as well as the respective normalized intensity. To create files with the data properly converted, a function was made in *Python 3.6.3*. The code is in Appendix D.

To obtain the real and imaginary part of the dielectric function a HORIBA-Jobin Yvon Uvisel spectroscopic ellipsometry system was used with an incident angle of 70° and in a spectral range between 1.5 and 6.5 eV. The acquired data was analysed with *DeltaPsi 2* software (HORIBA) and all error functions of the performed fits can be found in the Appendix C.

The models used to analyse the SE data were composed by the following layers: crystalline silicon as a substract, SiO_2 (silicon native oxide), the material to be analysed and a roughness layer (50 % of void and 50 % of the material) (Figure E.1). For the crystalline silicon it was used a reference model of the software. The model of the SiO_2 was fitted using the Tauc-Lorentz dispersion formula [13] at the same time as its thickness (with an initial guess of 20 Å) from a silicon wafer. Then, that model of the SiO_2 was used in all samples without fitting. For the films to be analysed both the parameters of the Tauc-Lorentz dispersion formula [13] and thickness were fitted. The initial guesses for the thicknesses were the thicknesses obtained by the other techniques or the values one expected from the fabrication methods. In the samples where the thickness of the roughness layer was close to 0.1 Å the layer was not used because that is the lower result of a thickness fitting, so it is meaningless.

In order to have a more direct measurement of the roughness of the film, Atomic Force Microscopy (AFM) analyses were performed using Asylum MFP-3D system in tapping mode. The AFM images analysis were done in the *Gwyddion* software. Also, to have a more direct measure of some film thicknesses, a XP-200 profilometer from Ambios Technology were used. The compositions of the films were obtained by Rutherford Backscattering Spectrometry (RBS) using a 2.5 MV van de Graaf Accelerator with a 2 MeV He^+ beam. The RBS spectra were analysed with the IBA DataFurnace NDF software [43]. All error functions of the performed fits are in Appendix C.

The characterization of the Metal-Insulator-Semiconductor (MIS) devices were performed in Keysight B1500A Semiconductor Device Analysis. A scanning range from 5 to −11 V with a frequency of 100 kHz were used. The metal contact was made of molybdenum and was the grounded contact (Figure E.2).

2.2 Materials fabrication

2.2.1 Ta_2O_5 samples deposition process

The first samples to be analysed were Ta_2O_5 films. With this samples one aimed to study the influence of rf power in the Ta_2O_5 target in the density and roughness of the films and to assess how XRR can be used to extract information. In order to achieve that, six samples were prepared with a range of 0.31 to 1.85 $W\,cm^{-2}$ rf power in the Ta_2O_5 target.

All films were deposited in pieces of a 4″ p-type silicon wafer with a resistivity from 1 to 2 Ω cm by rf sputtering from a 2″ Ta_2O_5 target. The deposition pressure was 0.3 Pa and a flow ratio of Ar/O_2 was 14/1. It was also used a 15 W sample bias.

A piece of the same wafer was analysed to obtain the SiO_2 thickness. The goal was to be sure of the most amount of properties possible so one has less fitting parameters in the SE and XRR data analysis.

2.2.2 Ta_2O_5/SiO_2 samples deposition process

Two sets of samples were produced with two different objectives. The main goal was to produce films to be used as the dielectric material in transistors and in MIS capacitors. Here a thickness of 250 nm were desired for the dielectric layer. In order to achieve that, a first set of samples were fabricated to calculate the growth rate of the films. Knowing the growth rate, a second set of samples were produced with the desired thickness of 250 nm.

The deposition process of these samples was similar to the Ta_2O_5 samples. Nevertheless these films were deposited by rf co-sputtering from a 2″ Ta_2O_5 and a 2″ SiO_2 AJA systems targets. Besides that, six samples for each set were produced with a rf power of 1.23 $W\,cm^{-2}$ in the SiO_2 target and in a range of 0.31 to 1.85 $W\,cm^{-2}$ in the Ta_2O_5 target. A sample with only Ta_2O_5 was also produced with a rf power of 1.23 $W\,cm^{-2}$.

2.2.3 ZTO samples deposition process

In order to study the influence of hydrogen in ZTO films to be used as the dielectric layer in TFTs, several films were produced at different fabrication conditions.

All films were fabricated in a 4″ p-type silicon wafer with a resistivity from 1 to 2 Ω cm by rf sputtering from a 2″ ZTO AJA systems target. The time of pre-sputtering used was 15 min, the deposition pressure of 0.3 Pa with 50 sccm of Ar flow. The conditions that changed between samples were: the rf power in the target (combined with a change of the deposition time) and the flow of both O_2 and H_2.

Chapter 3

Results and discussion

3.1 Ta_2O_5 films

The first set of samples considered here consisted of Ta_2O_5 films grown by rf sputtering on silicon. These films are usually used as the dielectric layer in devices such as TFTs at Materials Research Center (CENIMAT). This set of samples was produced with different rf powers (from 0.3 to 1.85 $W\,cm^{-2}$) in the Ta_2O_5 target during the sputtering process and using a substrate bias of 15 W. With this it was aimed to study the influence of the rf power in the fabricated films.

In the following table it is possible to found the nomenclature used in the section. The nomenclature was chosen in function of the rf power.

Table 3.1: Nomenclature of the Ta_2O_5 samples.

Sample	Rf power ($W\,cm^{-2}$)
Ta1	0.30
Ta2	0.62
Ta3	0.93
Ta4	1.23
Ta5	1.54
Ta6	1.85

Before the characterization of the Ta_2O_5 films, a piece of the same silicon wafer was characterized. The objective was to lower the number of the fitting parameters of the data analysis. The analysis of the silicon wafer can be found in Appendix F. With that analysis one concluded that it is possible to use a native oxide thickness of 20 Å in the SE data analyses.

An important remark about the XRR is that it was used the theoretical SLD of Si and SiO_2: 18.886×10^{-6} and 20.124×10^{-6} Å^{-2}, respectively (more details in Appendix F). The XRR data was analysed using the procedure presented in Appendix B.

In Figure 3.1 it is possible to see the measured data of two samples with the respective fits: the sample with a low rf power (Ta2) and the sample with a high rf power (Ta6). Just with this figure it is noticed that the sample Ta1 should have a similar density to the sample Ta6 because it has a similar critical angle (α_c). However, it has a bigger distance between two peaks of the Kiessing fringes (d_K) so it is clearly thinner. The results of the fits will be shown and discussed below in more detail but only with the measured data one can already conclude that the increase of rf power seems to originate thicker films.

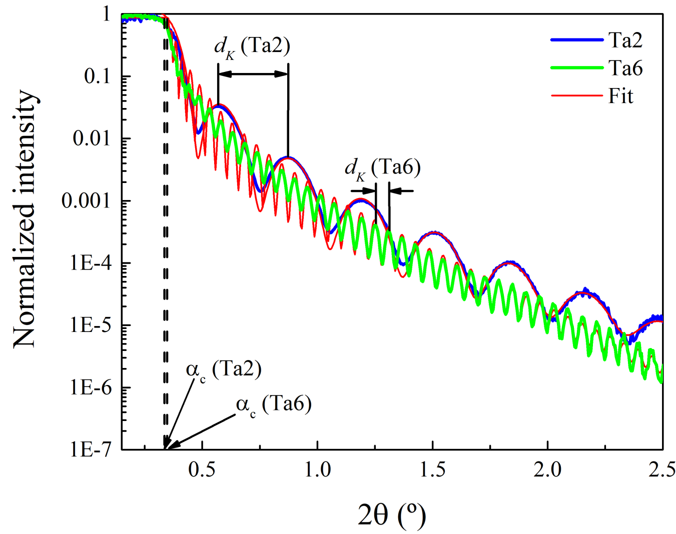

Figure 3.1: Measured data by XRR and respective fits of Ta1 and Ta6 samples.

The first parameter that will be discussed is the thickness of the Ta_2O_5 films. The obtained thicknesses are shown in Table 3.2. As one can see both techniques are in excellent agreement and the results for the thickness have a very low uncertainty. This is the first sign of the success of the implementation of XRR. Nevertheless, it is worth to point out a discrepancy in the case of the thickness of the Ta1 sample. This will be discussed later.

Table 3.2: Thicknesses obtained from Ta_2O_5 samples by XRR and SE using 20.0 Å as thickness in the SE data analysis.

Sample	Deposition time (min)	Ta_2O_5 thickness (Å)		Ta_2O_5 growth rate (Å/min)		SiO_2 thickness (Å)
		XRR	SE	XRR	SE	XRR
Ta1	30	19.1 ± 0.4	28.9 ± 0.3	0.64	0.96	17 ± 8
Ta2	30	133.3 ± 0.9	136 ± 2	4.4	4.5	18 ± 3
Ta3	26	316 ± 2	319 ± 2	12.2	12.3	18 ± 11
Ta4	20	238.2 ± 0.6	232 ± 2	11.9 [1]	11.6 [1]	17 ± 3
Ta5	20	573 ± 1	572 ± 3	28.7	28.6	18 ± 5
Ta6	20	718 ± 2	718 ± 5	35.9	35.9	19 ± 6

[1] The flow ratio of Ar/O_2 used to grow this sample was 14/3 instead of 14/1 and this may be the explanation for a smaller growth ration.

To have a better view of the differences between the thicknesses obtained by SE and XRR, a representation of the thicknesses obtained by both techniques is presented in Figure 3.2. A linear fit was performed in order to compare these differences with the results reported in the literature (witout the thickness of Ta1 sample). The result of this fit revealed to be similar to the ones described in the literature [11, 44–46]: there is a clear

linear tendency and the slope of the linear fit is near 1. Besides that the interception is equal to 0.

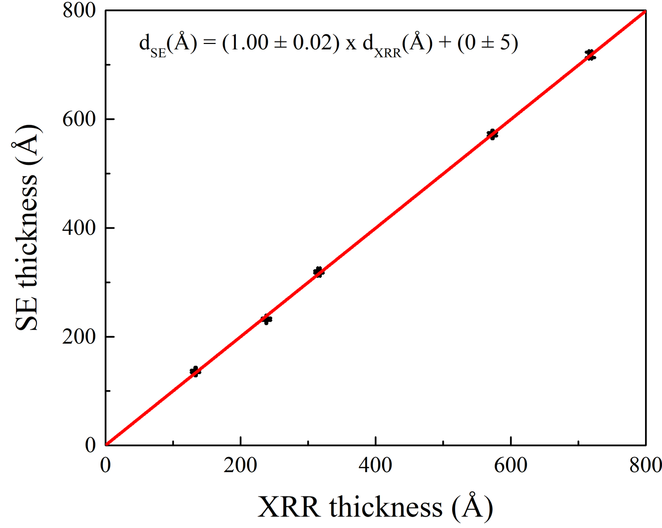

Figure 3.2: Comparison between the thicknesses obtained from XRR and SE.

Besides the thickness of the Ta_2O_5, the thickness of the native oxide was also fitted in the XRR data analysis. The results (see Table 3.2) are very consistent between samples when one takes in consideration the associated uncertainty. Not only that, but the results are also similar to the 20 Å used as the thickness of the native oxide in SE data analysis.

The thicknesses of both the Ta_2O_5 and the native oxide were not the only fitted parameters. The SLD and roughness of the samples were also fitted. Previously, with only the representation of the XRR data of the samples Ta2 and Ta6 (Figure 3.1) one concluded that the density should not be changing with the increase of the rf power in the target.

In Table 3.3 the results of the fits are presented and the same conclusion can be taken: no evidence of a change in the density of the samples was found for different values of rf power. This is true not only for the density, but also for the roughness of the films that were obtained by XRR and AFM (here SE did not give viable results).

Table 3.3: The roughness obtained by XRR and AFM and the SLD obtained by XRR using Si and SiO_2 SLD values of 18.886×10^{-6} and 20.124×10^{-6} $Å^{-2}$ respectively.

Sample	SLD (10^{-6} $Å^{-2}$)	Ta_2O roughness (Å)	
	XRR	XRR	AFM
Ta1	48 ± 9	5.0 ± 0.5	2.8
Ta2	49 ± 3	3.4 ± 0.2	4.2
Ta3	48 ± 3	4 ± 2	4.2
Ta4	48 ± 2	5.1 ± 0.5	3.7
Ta5	50 ± 4	5 ± 2	3.3
Ta6	48 ± 4	5 ± 2	3.5

From the AFM images used to get the roughness of the samples, one can see how smooth and regular the surfaces of the films are. As an example, two of those images are show below. The small dots in the surfaces may be impurities acquired by the exposition of the samples to the air.

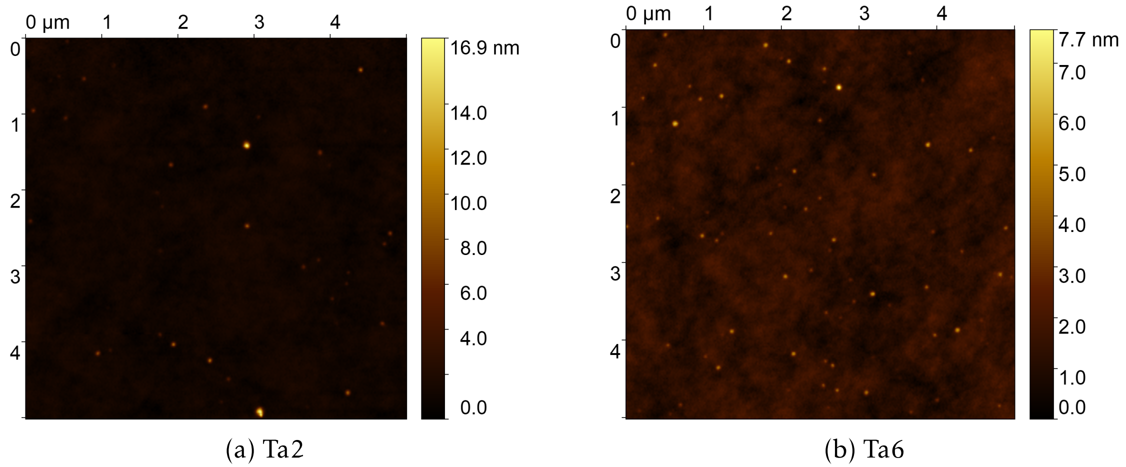

(a) Ta2

(b) Ta6

Figure 3.3: Images of the surfaces of two samples obtained by AFM.

As previously said, with the XRR analysis one concluded that the SLD of the samples did not change with the variation of the rf power. In other words, the density remained unchanged. The same conclusion can be made with the analysis of the Tauc-Lorentz models obtained to describe the samples. This is shown in Figure 3.4 where the real and imaginary part of the dielectric function (ε_1 and ε_2, respectively) are represented as functions of the photon energy. The models for these two properties are very similar for all samples, except for the Ta1 sample(Table H.1). This may be the reason for the difference in the thickness determined by SE and XRR of this sample.

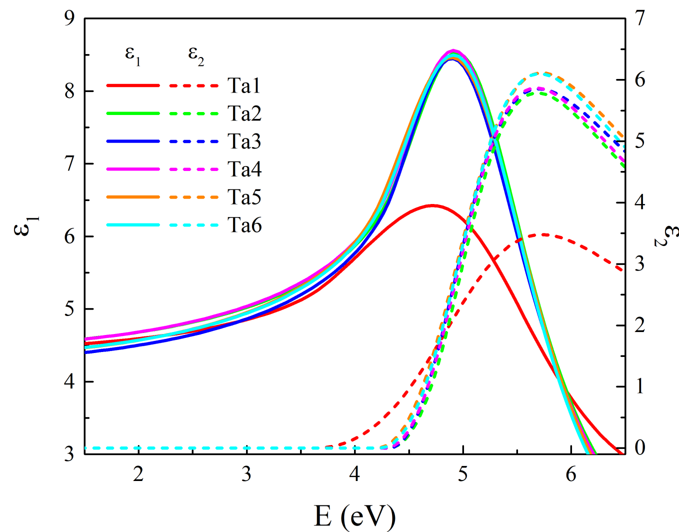

Figure 3.4: Real and imaginary part of the dielectric function obtained by SE.

For the other samples a change in density is not found, as the maximum of ε_2 does not clearly change [47]. Besides that, it is possible to notice that in all samples the Ta_2O_5 is amorphous, because the increase of the ε_2 with the photon energy is not abrupt [26].

Furthermore, from the parameters of the Tauc–Lorentz model (Table H.1) it is possible to conclude that the increase of the rf power in the Ta_2O_5 target leads to a small decrease of the band gap of the films and a decrease of short-range order (increase in C) [17, 47]. Again, no difference in the parameter A was found, so the density of the films did not change with different values of the rf power in the Ta_2O_5 target [17, 47], which is consistent with the results of the XRR data analysis.

To summarise, with this set of Ta_2O_5 samples grown by rf sputtering it was possible to conclude that: no difference in the density and roughness of the films was found with the variation of rf power in the Ta_2O_5 target, the increase of the rf power decreased the band gap and short-range order of the films and all samples were amorphous.

3.2 TaSiO samples

After the successful implementation of XRR and the use of the procedure presented in Appendix B to characterize Ta_2O_5 films, one aimed to use this technique to characterize more complex samples. So, the second and third sets of samples that were characterized consisted in a mixture of Ta_2O_2 and SiO_2 compound films (TaSiO) for a dielectric study performed in CENIMAT. The films were grown by co-sputtering and different rf powers were used on the Ta_2O_2 target to achieve samples with different compositions.

Two sets of samples were analysed: films used to determine the growth rate of the specific target powers (named gr-TaSiO) and films used for the dielectric layer in TFTs and MIS devices, where the thickness of all layers were set to be approximately 250 nm (named d-TaSiO). In the following table the nomenclature and the details of the deposition process of each sample is presented. The used nomenclature was set based on the rf power and composition of each sample.

Table 3.4: Nomenclature of both gr-TaSiO and d-TaSiO samples.

Sample		Rf power ($W\,cm^{-2}$)	
growth rate determination	dielectric layer	Ta_2O_5 target	SiO_2 target
gr-Ta1Si	-	0.30	1.23
gr-Ta2Si	d-Ta2Si	0.62	1.23
gr-Ta3Si	d-Ta3Si	0.93	1.23
gr-Ta4Si	d-Ta4Si	1.23	1.23
gr-Ta5Si	d-Ta5Si	1.54	1.23
gr-Ta6Si	d-Ta6Si	1.85	1.23
gr-Ta4	d-Ta4	1.23	0

3.2.1 Growth rate determination (gr-TaSiO samples)

Since these samples were produced to determine the growth rate, the thickness is the most important parameter to be measured. For this set of samples four techniques were used to do so: profilometry, XRR, SE and RBS.

As in the previous section, an important remark about the XRR needs to be done. Since the fit of the SLD of the native oxide and silicon were not possible to perform, the theoretical SLD of Si and SiO_2 used were 18.886×10^{-6} and 20.124×10^{-6} Å^{-2} respectively (more details in Appendix F). Despite that it is possible to see in Figure 3.5 de quality of the fits. Just with the information found in the figure below, it is possible to predict that the increase of rf power in the Ta_2O_5 leads to thicker samples because the sample gr-Ta6Si has a bigger distance between two peaks of the Kiessing fringes (d_K) and leads to denser samples since the critical angle (α_c) is higher in the sample gr-Ta6Si.

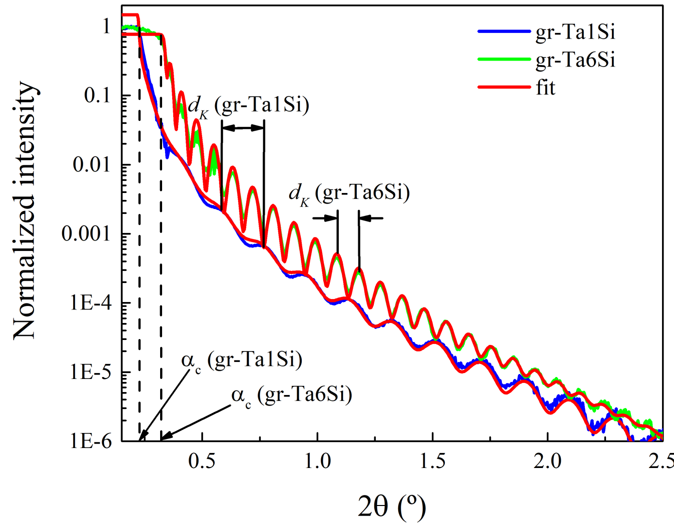

Figure 3.5: Measured data and fit of the samples gr-Ta1Si and gr-Ta6Si.

Taking this remark in mind for the XRR data analysis the thickness in length units is a parameter that can be fitted. The same happens in the SE data analysis. For the other techniques the thickness is obtained in a different way. On one hand, by profilometry the thickness is obtained directly with the measure in length units. On the other hand, with RBS the thickness is a fitting parameter, but it is expressed in atoms cm^{-2} and to be converted to length units one must to consider the film's density.

The RBS spectra with the obtained fits with the energy barriers indicated for each element is shown in Figure 3.6. It was needed to assume a fixed stoichiometry for the tantalum and silicon oxides in order to extract a relative concentration of each oxide. In other words, the fit was not done for the elements but for the molecules (it was assumed that the both components formed a solid solution). Looking at the figure bellow one can see that the number of counts for the peak of Ta is increasing with the increase of the rf power in the target. This means that the quantity of Ta is also increasing.

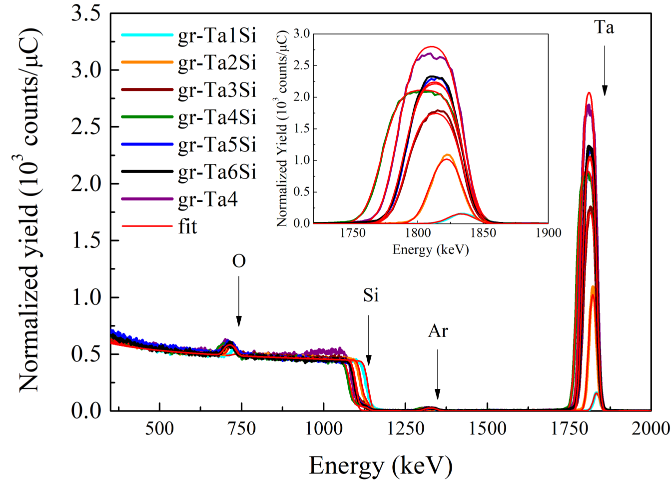

Figure 3.6: RBS spectra from all samples with the respective fits in red.

The same result can be seen in Table 3.5 where the results of the fits are presented. The molecular % of Ta_2O_5 is increasing relatively to the molecular % of SiO_2. The molecular % of Ar remains between 3 and 5 % for almost all samples.

Table 3.5: Results of the RBS fits.

Sample	Thickness (atoms cm^{-2})	Ta_2O_5 (%)	SiO_2 (%)	Ar (%)
gr-Ta1Si	38.0	25.5	66.4	8.1
gr-Ta2Si	251.0	31.4	65.8	2.8
gr-Ta3Si	374.0	40.8	40.8	3.8
gr-Ta4Si	500.0	67.3	29.1	5.0
gr-Ta5Si	377.5	70.1	25.5	3.3
gr-Ta6Si	376.4	72.0	24.5	3.5
gr-Ta4	390.0	95.2	-	4.8

However, as previously said, since one wants to compare the thickness obtained by this technique with the others it is fundamental to convert the thickness from atoms cm^{-2} to length units, in this case Å. To do so the procedure in Appendix G was followed. One needs to take in mind that for the conversion it was necessary to use the mass densities of the components 2.2 and 8.2 g cm^{-3} for the Ta_2O_5 and SiO_2, respectively [48].

With this conversion it is possible to show the thicknesses for all techniques in Table 3.6. The first conclusion is that all techniques are in general agreement. The profilometry revealed to be the less accurate technique to measure these films, as expected. It is also noticeable that for the gr-Ta1Si and gr-Ta2Si samples it was not possible to get a good model to describe the measured SE data and the results for these two samples are not accurate. This will be discussed in more detail below. Furthermore, for the thinner sample (gr-Ta1Si) the fit of the RBS data does not agree with the other techniques. That can be

explained by the difficult fitting of the measured data of films with such a low thickness.

Table 3.6: Thicknesses obtained by profilometry, XRR, SE and RBS.

Sample	Film thickness (Å)			
	profilometry	XRR	SE	RBS
gr-Ta1Si	(24 ± 3) × 10	212 ± 4	0.20 ± 0.05	55 ± 3
gr-Ta2Si	(32 ± 4) × 10	330.8 ± 0.5	266 ± 4	358 ± 18
gr-Ta3Si	(57 ± 3) × 10	497 ± 4	507 ± 3	511 ± 26
gr-Ta4Si	(73 ± 5) × 10	672 ± 5	678 ± 5	670 ± 34
gr-Ta5Si	(52 ± 4) × 10	451 ± 4	462 ± 2	503 ± 26
gr-Ta6Si	(46 ± 3) × 10	445 ± 4	458 ± 2	501 ± 26
gr-Ta4	-	505 ± 2	507 ± 4	-

Despite the results being similar, the thickness from RBS are slightly different in some cases relatively to the thicknesses obtained by XRR and SE. Three main reasons can be pointed out. The first one is that the fits were from the molecules and not the elements and the stoichiometry can be different from the stoichiometry assumed. The second one is that the mass density assumed may not be the right one. Finally, the fits are not perfect and one sign of that is that the molecular % of Ar is not consistently increasing with the increase of the rf power. Nevertheless, the difference between techniques is very small.

With the thicknesses determined it is possible to calculate the growth rates as one can see in Table 3.7. At the time the d-TaSiO samples were fabricated, only the thicknesses obtained by profilometry were known. This does not represent a problem because the growth rates calculated based on the four techniques are very close to each other.

Table 3.7: Calculated growth rates based on the obtained thicknesses.

Sample	Deposition time (min)	Growth rate (Å/min)			
		profilometry	XRR	SE	RBS
gr-Ta1Si	30	8.0	7.1	-	1.8
gr-Ta2Si	30	10.7	11.0	-	11.9
gr-Ta3Si	30	19.0	16.6	16.9	17.0
gr-Ta4Si	30	24.3	22.4	22.6	22.3
gr-Ta5Si	15	34.7	30.1	30.8	33.5
gr-Ta6Si	12	38.3	37.1	38.2	41.8
gr-Ta4	30	-	16.8	16.9	-

Although the main objective has already been achieved, more analyses can be done with these samples. One relation that can be study is the relation between the thicknesses obtained by XRR and SE data analysis presented in Figure 3.7. The result is similar to the results reported in literature [11, 44–46]: there is a clear linear tendency, the slope of the

linear fit is near 1 and the interception is different than 0. Interceptions different than 0 have been reported in different studies but this fact remains without a good explanation [45].

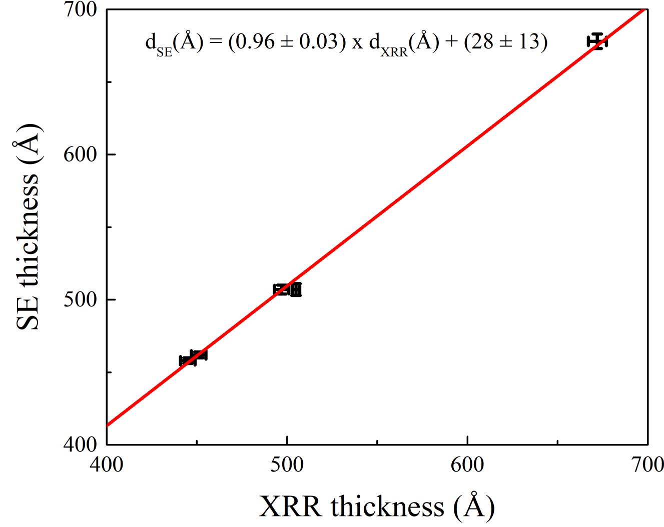

Figure 3.7: Comparison between thicknesses obtained from XRR and SE.

Continuing the comparison between XRR and SE results, an agreement is not found in the roughness of the films (Table 3.8). The roughnesses obtained by XRR seems to be very similar for all samples. The same does not happen with the SE data analysis. Not only that, but by SE it was not possible to determine the roughnesses of some films because those values tended to 0.1 Å, which is the limit of the used software, so those values were meaningless. In those cases, no roughness layer was used in the data analysis. Here XRR revealed to be a more useful technique to measure the film roughness.

Table 3.8: Results from XRR and SE data analysis of the Ta_2O_5 and of the native oxide using Si and SiO_2 SLD values of 18.886×10^{-6} and 20.124×10^{-6} Å^{-2} respectively.

Sample	Film roughness (Å)		SLD	SiO_2 thickness (Å)		SiO_2 roughness (Å)
	XRR	SE	XRR	XRR	SE	XRR
gr-Ta1Si	4.1 ± 0.3	-	20.0 ± 0.9	12 ± 3	249.9 ± 0.4	13 ± 2
gr-Ta2Si	4.4 ± 0.6	-	30 ± 2	27 ± 3	70 ± 3	15.8 ± 0.9
gr-Ta3Si	4 ± 1	-	37 ± 2	25 ± 4	35 ± 2	13 ± 4
gr-Ta4Si	4.9 ± 0.9	6 ± 2	39 ± 2	23 ± 5	22 ± 4	16 ± 8
gr-Ta5Si	3 ± 2	2.9 ± 0.7	41 ± 2	21 ± 5	30 ± 2	12 ± 6
gr-Ta6Si	6 ± 2	3.9 ± 0.8	41 ± 2	21 ± 6	32 ± 2	14 ± 6
gr-Ta4	4.0 ± 0.9	7 ± 1	50 ± 2	21 ± 7	62 ± 3	-

For the determination of the native oxide thickness, XRR revealed again to be a more

accurate technique. It is possible to see that the thicknesses of the native oxide were not in agreement for all samples for both techniques. In the case of the XRR, the results are close to the expected and, given the uncertainty, the results are close to each other. However, the results of the native oxide thickness obtained by the SE data analysis are not so reliable because of the incoherence between samples and in some cases, like in the sample gr-Ta4, is not even close to the expected values.

This incoherence highlights the importance of analysing a piece of the substrate in the first place. This can give the opportunity to reduce the number of the fitting parameters in the data analysis, like the native oxide thickness and roughness.

For the last conclusion of the XRR results, given the fact that Ta_2O_5 is a denser material than SiO_2 [48] it was predictable that, with the increase of Ta_2O_5 in the film, the film becomes denser. This is proven correct by the fact that both the SLD and the molecular % of Ta_2O_5 are increasing as the rf power in the Ta_2O_5 target increases (Table 3.5 and 3.8).

Previously in Tables 3.6 and 3.8 was evident that the models for the gr-Ta1Si and gr-Ta2Si do not give physically reliable results. The problem with the models of gr-Ta1Si and gr-Ta2Si is shown in Figure 3.8 and in Table H.2. There is a huge discrepancy between this two models and the other models. Despite the attempts, better models were not achieved.

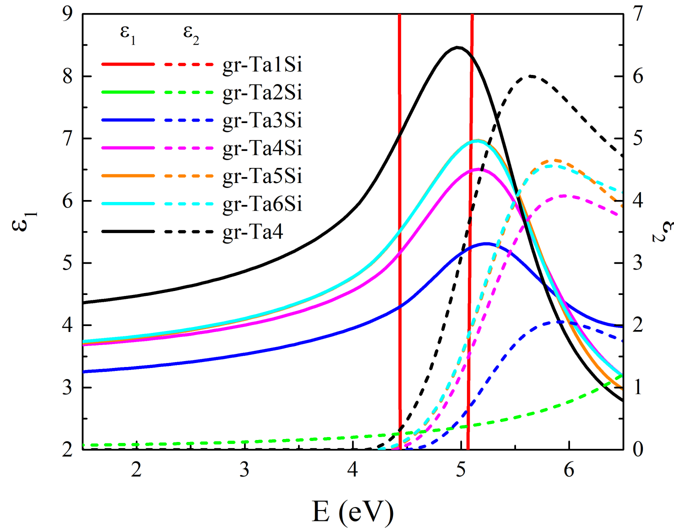

Figure 3.8: Real and imaginary part of the dielectric function of the samples.

With the representation of ε_1 and ε_2 it is possible to see that with higher concentration of Ta_2O_5 the peaks become more intense. This is also perceptible in Table H.2 where the parameter *A1* increases. This means that the films become denser [17, 47]. The parameter *C1* also increases with the concentration of Ta_2O_5 which reveals that the films have a decrease of short-range order with the increase of the rf power in the Ta_2O_5 target [17, 47] which contradicts the reported results [24]. However, the decrease of E_g with the increase of the Ta_2O_5 concentration is in agreement with the literature [24]. It is also possible to conclude that all Ta_2O_5 films are amorphous, because the increase of the ε_2 with the photon energy is not abrupt [26].

In summary, with this set of samples it was possible to conclude that the density, Ta_2O_5 composition and growth rate increase with the rf power in the Ta_2O_5 target at the same time as the short-range order decreases. Once again, the success of the implementation of XRR was demonstrated.

3.2.2 Dielectric layer (d-TaSiO samples)

After the characterization of the gr-TaSiO samples to calculate the growth rate, the characterization of the d-TaSiO samples will be presented. The first part of this characterization is the analysis of the thickness, roughness and composition of the film and of the native oxide. The second part to be shown is the electric characterization of the films as a dielectric layer in a MIS structure.

In this section the thicknesses were obtained by two techniques: SE and RBS. The results are presented in Table 3.9. The deposition time used to fabricate these samples was based on the growth rate calculated using the thicknesses obtained by profilometry (Table 3.7). With the exception of the sample d-Ta3Si, all samples have a thickness close to the desired 250 nm. Besides that, as have been noticed, the results for both techniques are very close to each other. This agreement can lead us to two other conclusions.

Table 3.9: Thicknesses obtained by SE and RBS.

Sample	Film thickness (Å)		Film thickness (atoms cm^{-2})
	SE	RBS	RBS
d-Ta2Si	2395 ± 14	$(236 \pm 12) \times 10$	1668
d-Ta3Si	2049 ± 7	$(204 \pm 11) \times 10$	1495
d-Ta4Si	2425 ± 8	$(241 \pm 13) \times 10$	1796
d-Ta5Si	2311 ± 10	$(228 \pm 12) \times 10$	1712
d-Ta6Si	2550 ± 11	$(256 \pm 13) \times 10$	1923
d-Ta4	2520 ± 13	$(237 \pm 12) \times 10$	1855

First it is important to take in mind that in order to calculate the thicknesses from the RBS results it was assumed the mass density of the SiO_2 and Ta_2O_5 of 2.2 and 8.2 g cm^{-3}, respectively. Not only that, but it is fundamental to understand that the fits were done assuming that the components of the films were Ta_2O_5, SiO_2 and Ar (although Ar is not used to calculate the thicknesses). This means that the results presented are the results of the fit with the molecules and not the fit with the elements (Appendix G).

Therefore, if the results of both techniques are so similar with these assumptions, it means that the assumed stoichiometry may be close to the real stoichiometry of the components of the films and that the components have a density close to the bulk densities.

To calculate the thickness presented in Table 3.9 obtained by RBS, the thickness in atoms cm^{-2} and the composition of the films were used. The composition obtained by

RBS and SE is shown in Table 3.10. The results are the expected ones: with the increase of the rf power in the Ta_2O_5 target the concentrations of Ta_2O_5 and Ar increase.

Table 3.10: Composition in molecular % obtained by RBS and SE data analysis.

Sample	RBS			Normalized RBS	SE
	Ta_2O_5 (%)	SiO_2 (%)	Ar (%)	Ta_2O_5 (%)	Ta_2O_5 (%)
d-Ta2Si	37.5	59.1	3.4	38.8	40.6
d-Ta3Si	57.6	38.6	3.8	59.9	56.4
d-Ta4Si	65.7	30.0	4.3	68.7	60.5
d-Ta5Si	70.6	25.0	4.5	73.8	61.5
d-Ta6Si	71.7	24.0	4.3	74.9	66.3
d-Ta4	94.5	-	5.5	100	-

The results were the expected because on one hand in the RBS data (Figure 3.9) the peak of the Ta also increases with the increase of the rf power. This means that the quantity of Ta is also increasing. On the other hand, the trapping of rare gases in sputtering is proportional to the atomic mass of the targets. Since Ta_2O_5 has a higher atomic mass than SiO_2, with the increase of the molecular % of Ta_2O_5, more Ar atoms are trapped in the deposited film [49].

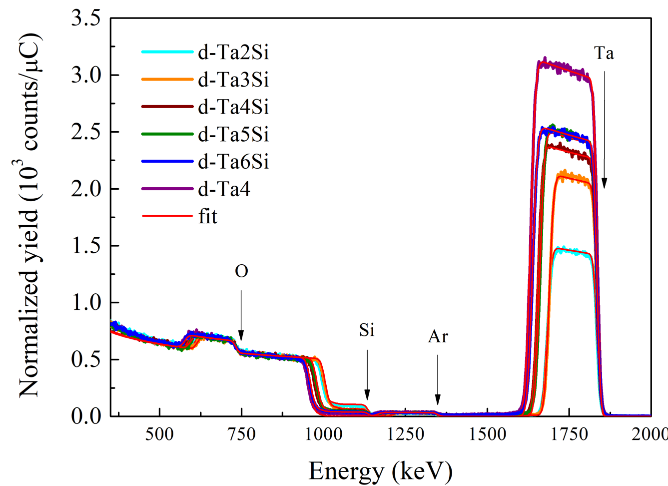

Figure 3.9: RBS spectra from all samples with the respective fits in red.

Also in Table 3.10 it is compared the molecular % of the Ta_2O_5 obtained by RBS and SE. In this comparison it was used a normalised concentration in the RBS data analysis. The normalised concentration only takes into account the concentration of Ta_2O_5 and SiO_2. This was used because not only it is not possible to calculate the thickness with films that have gases in its constituents, but also because in the SE data analysis presented here, Ar were not considered as well.

The molecular % of the Ta_2O_5 presented for the SE data analysis was calculated too. Using a different model (Figure E.3), the volumetric concentration of the Ta_2O_5 was fitted. The mass densities were assumed to calculate the molecular %. Knowing that RBS gives more viable results, one can conclude that it is possible to obtain a concentration with SE, but the result can only be used to give an idea of the concentrations and cannot be assumed as a certain result. This is the case because in these analyses the concentration of Ta_2O_5 and the Tauc-Lorentz model of Ta_2O_5 were fitted at the same time.

Besides the thickness and composition, SE give more information, namely the thickness of the silicon oxide and the roughness of the Ta_2O_5 films. However, as one can see in the table below (Table 3.11), the models obtained by SE revealed to be not very accurate for these two parameters. On one hand, the values of the native oxide thickness are not similar between samples. On the other hand, the roughness could not be obtained for two samples and is not consistent in the others. Nevertheless, it seems that the thickness of the Ta_2O_5 was not affected by these problems. Nevertheless, the parameters of the Tauc-Lorentz models can give more information (Figure 3.10 and Table H.3)

Table 3.11: Thicknesses of the native oxide and roughnesses of the Ta_2O_5.

Sample	SiO_2 thickness (Å)	Ta_2O_5 roughness (Å)
d-Ta2Si	14 ± 8	NS
d-Ta3Si	22 ± 3	NS
d-Ta4Si	9 ± 3	5 ± 2
d-Ta5Si	16 ± 4	8 ± 2
d-Ta6Si	18 ± 4	4 ± 2
d-Ta4	21 ± 5	11 ± 2

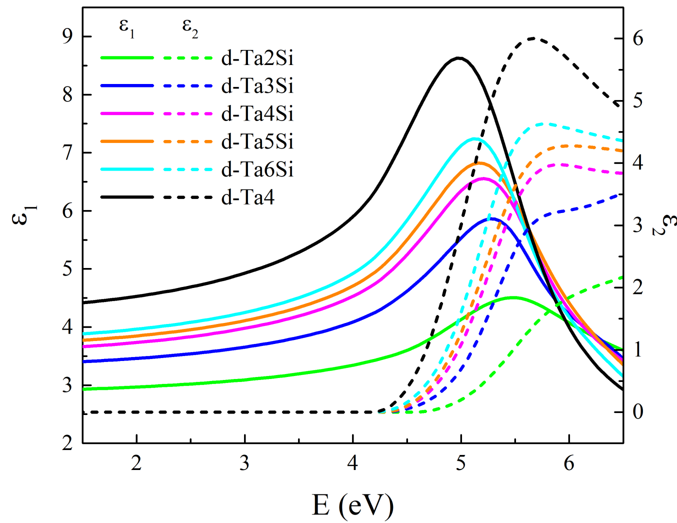

Figure 3.10: Real and imaginary part of the dielectric function of the samples.

To conclude the first part of the characterization of the d-TaSiO samples one may look to the results of the Tauc-Lorentz models. Those results are in line with the results of the gr-TaSiO samples: the films become denser and have a decrease of short-range order with the increase of the rf power in the Ta_2O_5 target and all films are amorphous. This is shown in both Figure 3.10 and Table H.3.

The second part of this characterization consisted in the electrical characterization of MIS structures using the d-TaSiO films as dielectric layers. Therefore, the capacitance was measured as a function of the frequency (capacitance characteristic) and voltage.

The objective of the study of these films was to use them as the dielectric layer in transistors. So, the possibility of measuring these films in high frequency was desired. However, as one can see in Figure 3.11 for frequencies higher than 100 kHz the capacitance starts to increase. This effect is due to the high impedance of the cables. Because of that, the remain electrical tests were performed using a frequency of 100 kHz.

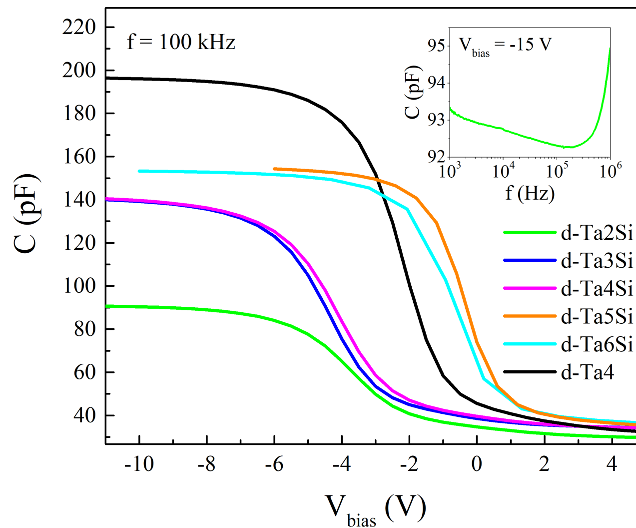

Figure 3.11: Electrical measurements of the d-TaSiO samples.

To know the dielectric constant of the films the capacitance was measured in function of the applied potential, as shown in the figure above. Knowing that the contacts' size was 494 µm × 494 µm, using the thicknesses obtained by SE (Table 3.9) and with the maximum capacitance of the films (Figure 3.11), the dielectric constant was calculated.

To get a better understanding of the calculated dielectric constants, the results are presented in Figure 3.12. As it is possible to see there, the dielectric function increases with the increase of molecular % of Ta_2O_5 in the films (caused by the increase of the rf power in the Ta_2O_5 target). The results are in agreement with the expected ones. The dielectric constants of SiO_2 and amorphous Ta_2O_5 are 3.9 [50] and 22-25 [51, 52], respectively. So, with the increase of the molecular % of Ta_2O_5, the dielectric constant of the films gets closer to the dielectric constant of the amorphous Ta_2O_5.

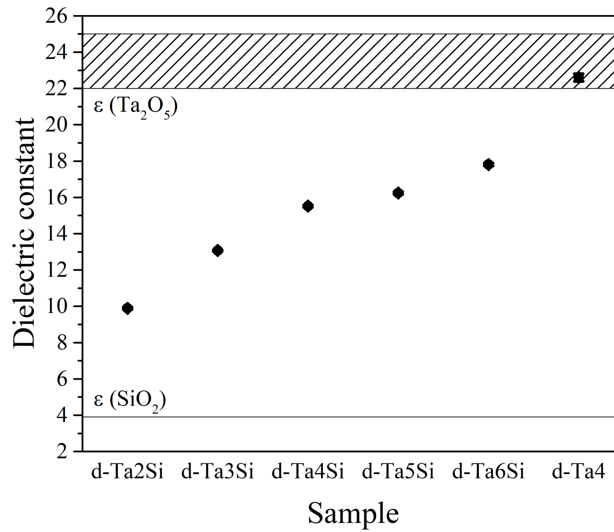

Figure 3.12: Dielectric constants obtained from the electrical measurements.

In conclusion, with these sets of samples of films with different mixtures of Ta_2O_5 and SiO_2 was possible to see that the films become denser and have a decrease of short-range order with the increase of the rf power in the Ta_2O_5. Is was also possible to conclude that with the increase of the rf power the molecular % of Ta_2O_5 also increased which lead to an increase of the dielectric constant.

3.3 ZTO samples

The final set of samples characterized was a set of ZTO films grown by rf sputtering. These samples were fabricated at the same time as the samples used by C. Fernandes *et al.* as the dielectric layer in TFTs for flexible electronics [34]. Here the objective was to understand the role of some fabrication parameters, namely the rf power in the ZTO target and the flow of O_2 and H_2. The nomenclature used is presented in Table 3.12.

Table 3.12: Samples nomenclature used in function of the fabrication parameters.

Sample	Rf power ($W\,cm^{-2}$)	H_2 flow (sccm)	O_2 flow (sccm)
P1-H1-O2	1	0	5.36
P1-H2-O2	1	0.5	5.36
P1-H3-O2	1	1	5.36
P2-H1-O1	2	0	1.78
P2-H1-O2	2	0	5.36
P2-H2-O2	2	0.5	5.36
P2-H3-O2	2	1	5.36
P2-H1-O3	2	0	10.72
P2-H2-O3	2	0.5	10.72
P2-H3-O3	2	1	10.72

In line with the other sections of this work, the XRR data was analysed using the procedure presented in Appendix B and once again the fit of the SLD of the native oxide and of the silicon were not viable. To solve this problem the assumed values of the SLD used for the Si and SiO_2 were 18.886×10^{-6} and 20.124×10^{-6} Å^{-2}, respectively. These values are the theoretical ones. A more detailed explanation of these problem can be found in Appendix F.

Nevertheless, and as in the previous sections, very good fits of the measures XRR data was obtained. In Figure 3.13 the real data and the fit of a sample is presented. This is a representative example because for the remain samples the quality of the fits was as good as the fit of this sample.

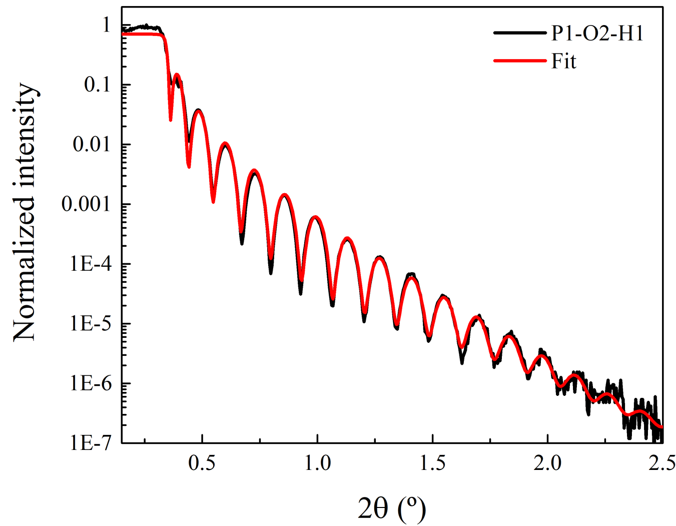

Figure 3.13: Real data and XRR fit of the sample P1-O2-H1.

To study the correlation of the thicknesses determined by both techniques, a comparison was made and it is presented in Figure 3.14. The result obtained with this comparison is similar to other results presented in this work as well as to the results reported in the literature [11, 44–46]. In other words, the result of the linear fit was a slope close to 1 and the interception is different than 0. As in the previous section, an explanation for the interception being different than 0 was not found.

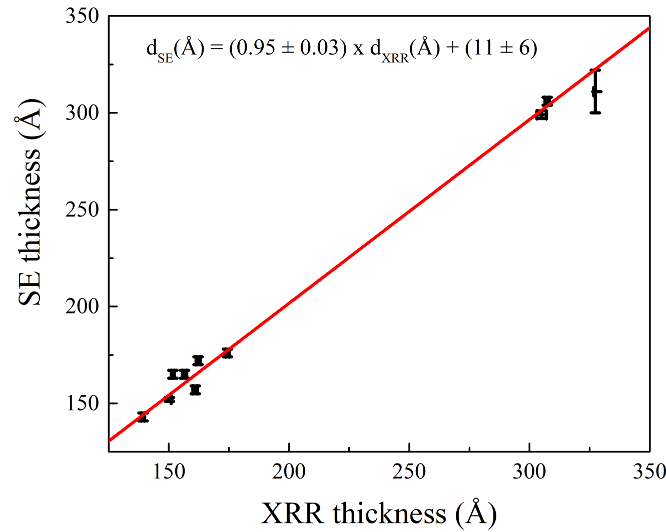

Figure 3.14: Comparison between thicknesses obtained from XRR and SE.

3.3.1 Influence of the rf power

The first parameter studied was the rf power in the ZTO target. Two different rf powers were tested: 1 W cm^{-2} (P1) and 2 W cm^{-2} (P2). Besides the change in the rf powers, the deposition time was also changed. In the samples where 1 W cm^{-2} was used, the deposition time was 20 min. The deposition time of the samples where 2 W cm^{-2} was used was 5 min. This means that using twice the rf power, the time used was a quarter. With this, half of the thickness was expected for the P2-samples compared to the P1-samples and that was the result, as one can see in Table 3.13. Besides that, it is noticeable that both techniques are in very good agreement.

Table 3.13: Results from XRR and SE data analyses of the samples with different target rf power using Si and SiO_2 SLD values of 18.886×10^{-6} and 20.124×10^{-6} Å^{-2}, respectively.

Sample	Film thickness (Å)		Film SLD (10^{-6} Å^{-2})	Film roughness (Å)
	SE	XRR	XRR	XRR
P1-O2-H1	299 ± 2	305 ± 5	44 ± 3	8 ± 2
P2-O2-H1	157 ± 2	161.1 ± 0.6	47 ± 3	6.4 ± 0.4
P1-O2-H2	311 ± 11	330 ± 3	45 ± 3	8 ± 2
P2-O2-H2	172 ± 2	161.5 ± 0.4	47 ± 3	6.0 ± 0.4
P1-O2-H3	306 ± 2	309 ± 3	44 ± 3	9 ± 2
P2-O2-H3	165 ± 2	156.0 ± 0.5	49 ± 3	6.4 ± 0.4

The differences between P1- and P2-samples are not just in the thicknesses. P2-samples also have a lower roughness, but this could be due to the fact that these samples

are thinner. To test this hypothesis, samples with similar thicknesses should be fabricated using different rf powers. Besides the roughness, the SLD also changes. The SLD increases with the increase of the rf power. Although the change is slight for the given uncertainties, it is possible to conclude that the density of the films increases with the increase of the rf power (supported by the increase of *A1* with the rf power shown in Table H.4).

The increase of the density is also confirmed by SE because as shown in Table H.4 the parameter $A1$ is also higher for P2-samples [17, 47]. Looking at the Tauc-Lorentz parameters for this sample is also possible to see an increase of the parameters $E1$ and $C1$. So, despite being denser, the sample also has a lower short-range order [17, 47]. With SE one can also conclude that the samples are amorphous, because as shown in Figure I.1 the ε_2 does not present an abrupt change with the photon energy [26].

3.3.2 Influence of the H_2 flow

The second parameter studied was the H_2 flow during the rf sputtering. To test the influence of this parameter, samples with three different flows were prepared. Some samples were fabricated without H_2 flow (H1), some with a flow of 0.5 sccm (H2) and others with a flow of 1 sccm (H3).

Starting with the thickness, one can see that the thicknesses are higher in the H2-samples. This may indicate that the use of H_2 flow in the fabrication of the samples can lead to higher thicknesses. Nevertheless, a critical point of H_2 flow may exist as the thicknesses are lower in the H3-samples than the H2-samples. More tests with more values of H_2 flow should be performed to obtain better conclusions. Besides that, it seems that the SLD increases with the H_2 flow but when one takes in consideration the associated uncertainty, that conclusion is not very clear.

Table 3.14: Results from XRR and SE data analyses of the samples with different H_2 flow using Si and SiO_2 SLD values of 18.886×10^{-6} and 20.124×10^{-6} Å^{-2}, respectively.

Sample	Film thickness (Å)		Film SLD (10^{-6} Å^{-2})	Film roughness (Å)
	SE	XRR	XRR	XRR
P1-O2-H1	299 ± 2	305 ± 5	44 ± 3	8 ± 2
P1-O2-H2	311 ± 11	330 ± 3	45 ± 3	8 ± 2
P1-O2-H3	306 ± 2	309 ± 3	44 ± 3	9 ± 2
P2-O2-H1	157 ± 2	161.1 ± 0.6	47 ± 3	6.4 ± 0.4
P2-O2-H2	172 ± 2	161.5 ± 0.4	47 ± 3	6.0 ± 0.4
P2-O2-H3	165 ± 2	156.0 ± 0.5	49 ± 3	6.4 ± 0.4
P2-O3-H1	165 ± 2	152.2 ± 0.9	43 ± 3	6.3 ± 0.9
P2-O3-H2	152 ± 1	150 ± 1	44 ± 3	6 ± 1
P2-O3-H3	143 ± 2	139.5 ± 0.8	46 ± 4	6.0 ± 0.7

Through the Tauc-Lorentz parameters (see Table H.5) no conclusions can be taken because no pattern was found in any parameter. The same happens looking at the representation of both parts of the complex dielectric function in Figure I.2, in which one can only conclude that all samples are amorphous [26].

3.3.3 Influence of the O_2 flow

Finally, the last parameter to be study was the influence of the O_2 flow during the fabrication process. Three different flows were tested to understand the role of the O_2 flow in the parameters of the samples: 1.78 (O1), 5.36 (O2) and 10.72 sccm (O3).

The results of the characterization of these samples can be seen in Table 3.15. A difference between the thicknesses was found. This difference may indicate that the increase of the O_2 flow results in a decrease of the thickness. The sample P2-O2-H1 is an exception for this hypothesis. To make a clear conclusion, more samples are needed to test this hypothesis. Besides the decrease of the thickness, the roughness and the SLD also present lower values for a higher O_2 flow. So, the increase of O_2 flow may lead to less dense and smoother films.

Table 3.15: Results from XRR and SE data analyses of the samples with different O_2 flow using Si and SiO_2 SLD values of 18.886×10^{-6} and 20.124×10^{-6} Å^{-2}, respectively.

Sample	Film thickness (Å)		Film SLD (10^{-6} Å^{-2})	Film roughness (Å)
	SE	XRR	XRR	XRR
P2-O1-H1	176 ± 2	175 ± 2	47 ± 3	6.7 ± 0.9
P2-O2-H1	157 ± 2	161.1 ± 0.6	47 ± 3	6.4 ± 0.4
P2-O3-H1	165 ± 2	152.2 ± 0.9	43 ± 3	6.3 ± 0.9
P2-O2-H2	172 ± 2	161.5 ± 0.4	47 ± 3	6.0 ± 0.4
P2-O3-H2	152 ± 1	150 ± 1	44 ± 3	6 ± 1
P2-O2-H3	165 ± 2	156.0 ± 0.5	49 ± 3	6.4 ± 0.4
P2-O3-H3	143 ± 2	139.5 ± 0.8	46 ± 4	6.0 ± 0.7

Looking at the Tauc-Lorentz parameters in Table H.6 and the dielectric function in Figure I.3 no tendency can be found. As a result of that, one can only conclude that all samples were amorphous [26].

Chapter 4

Conclusions and future perspectives

In this work the implementation of XRR at CENIMAT as a characterization technique of thin and ultra-thin films was the main objective. Through the use of the package *MOTOFIT 4.1* to analyse the measured data obtained from the diffractometer present at CENIMAT the objective was successfully achieved. Now it is possible to use this technique to measure the thickness, roughness and the SLD of thin films and ultra-thin films at CENIMAT.

The use of the SE as a complementary technique was also one of the objectives of this work. Using the ellipsometer of the CENIMAT and using Tauc-Lorentz dispersion formula this objective was also successfully completed. A very good agreement in the thicknesses measured by both techniques was found. In all groups of samples analysed in this work, a linear relation between the thicknesses obtained by XRR and SE data analyses was found. The slope of this relation for all set of samples was close to 1 and the interception was different than 0. In none of the group of samples analysed a good explanation for the slope being different than 0 was found.

RBS and profilometer analyses were also performed. An agreement was also found with the thicknesses obtained by these techniques. Besides the agreement between these four techniques, RBS and profilometer present some disadvantages. In order to calculate the thickness of a film with the RBS data the composition of the film must be well known, which does not always happen. The profilometer can give a direct measure of the thickness but it is less accurate and it is not suitable to measure ultra-thin films. So, XRR and SE can be more appropriate when RBS and profilometer cannot be carried out.

The use of XRR and SE as complementary techniques lead to very good results, being possible to say that these techniques work very well as complementary techniques. On one hand, throughout this work XRR was shown to be a better technique to determine the roughness of the films and to determine the thickness of the native oxide. On the other hand, SE can give more details about the films. Using the Tauc-Lorentz dispersion formula it was possible to compare the short-range order between films, to obtain the band gap of the films and to determine whether the films were amorphous or not.

All these conclusions resulted from the analysis of four groups of samples. The first group of those samples was Ta_2O_5 films. The second group of samples was prepared to know the growth rate of films with Ta_2O_5 and SiO_2 (TaSiO) in order to produce the third group of samples, in which 250 nm of thickness was desired. The final group of samples was ZTO films. All samples were produced by rf sputtering.

In the case of the Ta_2O_5 one aimed to study the influence of the rf power in the Ta_2O_5 target. One concluded that the films were amorphous and that the increase of the rf power in the Ta_2O_5 target lead to a decrease of the short-range order. No differences in the roughness or density were found.

From the TaSiO it was also studied the influence of the rf power in the Ta_2O_5 target.

The results showed that the films got a higher concentration of Ta_2O_5 and Ar, as predictable. The films, that revealed to be amorphous, got denser and the dielectric constant also increased with the increase of the rf power. On the other hand the short-range order decreased.

Samples with ZTO were produced in order to study the influence of the rf power in the ZTO target, the H_2 flow and the O_2 flow during the fabrication process. It can be concluded that all samples were amorphous according to the SE results.

The ZTO samples produced with higher rf power had a lower deposition time, so they were thinner. These samples revealed to have a lower roughness, but it was not clear if it was due to the use of higher rf power or due to the fact that these samples are thinner. Samples with similar thickness should be prepared to have a better understanding of the role of the rf power in the roughness of the films. It was also noticeable that the increase of the rf power lead to denser films and with lower short-range order.

The study of the use of H_2 flow indicates that it may have a role in the thickness of the film. For the intermediate value of flow the thickness were higher than for the lower and higher values of tested flows. This can mean that it may exist a critical point where the thickness has a maximum value. To be sure more samples with more values of H_2 flows should be characterized.

An increase of the O_2 flow lead to films less dense and with higher roughness. It seems that also lead to thinner films, but this conclusion is not clear. Here more tests are also desired to have a better understanding of the influence of the O_2 flow.

In the future, besides all the tests suggested above, other methods to analyse the XRR could be tested. The package *MOTOFIT 4.1* presents many advantages, but it showed some limitation for the analyses of thinner samples (below 30 Å). Besides that, *MOTOFIT 4.1* works within *IGOR*, which is a paid program. Once there are free alternatives, those alternatives must be studied. In this way, any CENIMAT's worker and student could analyse XRR data in their personal computer.

To test the use of the current analysis method more diverse samples should be analysed. Not only single layer but also multilayer systems. Samples with subtracts different from silicon and fabricated with different processes should also be characterized.

[1] V. Holý, U. Pietsch, and T. Baumbach. *High-Resolution X-Ray Scattering from Thin Films and Multilayers*. Vol. 174. Springer, 1999.

[2] L. Grave de Peralta. "Thin film characterization by X-Ray Reflectivity." Doctoral dissertation. Faculty of Texas Tech University, 2000, p. 77.

[3] M. Tolan. *X-Ray Scattering from Soft-Matter Thin Films*. Vol. 148. Springer, 1999, p. 191.

[4] A. Nelson. "Co-refinement of multiple-contrast neutron/X-ray reflectivity data using MOTOFIT." In: *Journal of Applied Crystallography* 39.2 (2006), pp. 273–276.

[5] F. Abeles. "Sur la Propagation des Ondes Electromagnetiques dans les Milieux Stratifies." In: *Ann. de Phys.* 3.3 (1948), pp. 504 –520.

[6] S. Lee, D. W. Jeong, and M. C. Choi. "Vertical order of DPPC multilayer enhanced by cholesterol-induced ripple-to-liquid ordered (LO) phase transition: Synchrotron X-ray reflectivity study." In: *Current Applied Physics* 17.3 (2017), pp. 392–397.

[7] S. R. Larsen, M. Hansteen, B. Pacakova, K. Theodor, T. Arnold, A. R. Rennie, G. Helgesen, K. D. Knudsen, H. N. Bordallo, J. O. Fossum, and L. P. Cavalcanti. *Sample cell for studying liquid interfaces with an in situ electric field using X-ray reflectivity and application to clay particles at oil–oil interfaces*. 2018.

[8] J. Jiang, K. Hirano, and K. Sakurai. "Interface-sensitive imaging by an image reconstruction aided X-ray reflectivity technique." In: *Journal of Applied Crystallography* 50.3 (2017), pp. 712–721.

[9] Y. Babanov, Y. Salamatov, and V. Ustinov. "A new interpretation of X-ray reflectivity in real space for low contrast multilayer systems I. Mathematical algorithm and numerical simulations." In: *Superlattices and Microstructures* 74 (2014), pp. 100–113.

[10] M. Baum, D. Rébiscoul, S. Tardif, N. Tas, L. Mercury, and F. Rieutord. "X-Ray Reflectivity analysis of SiO 2 nanochannels filled with water and ions: a new method for the determination of the spatial distribution of ions inside confined media." In: *Procedia Earth and Planetary Science* 17 (2017), pp. 682–685.

[11] A. Richter, R. Guico, and J. Wang. "Calibrating an ellipsometer using x-ray reflectivity." In: *Review of Scientific Instruments* 72.7 (2001), pp. 3004–3007.

[12] H. Fujiwara. *Spectroscopic Ellipsometry*. Ed. by Wiley. John Wiley & Sons Ltd, 2007.

[13] G. E. Jellison and F. A. Modine. "Parameterization of the optical functions of amorphous materials in the interband region." In: *Applied Physics Letters* 69.3 (1996), pp. 371–373.

[14] J. Tauc, R. Grigorovici, and A. Vancu. "Optical Properties and Electronic Structure of Amorphous Germanium." In: *physica status solidi (b)* 15.2 (1966), pp. 627–637.

[15] F. Wooten. *Optical Properties of Solids*. Ed. by A. Press. 1st Editio. New York, 1972.

[16] J. Robertson. "Band offsets of high dielectric constant gate oxides on silicon." In: *Journal of Non-Crystalline Solids* 303.1 (2002), pp. 94–100.

[17] L. Pereira, H. Águas, E. Fortunato, and R. Martins. "Nanostructure characterization of high k materials by spectroscopic ellipsometry." In: *Applied Surface Science* 253.1 SPEC. ISS. (2006), pp. 339–343.

[18] R. Degraeve, E. Cartier, T. Kauerauf, R. Carter, L. Pantisano, A. Kerber, and G. Groeseneken. "On the electrical characterization of high-κ dielectrics." In: *MRS Bulletin* 27.3 (2002), pp. 222–225.

[19] R. M. Wallace and G. D. Wilk. *High-κ Dielectric Materials for Microelectronics*. Vol. 28. 4. Taylor & Francis Group, 2003, pp. 231–285.

[20] J. M. Ngaruiya, S. Venkataraj, R. Drese, O. Kappertz, T. P. Leervad Pedersen, and M. Wuttig. "Preparation and characterization of tantalum oxide films produced by reactive DC magnetron sputtering." In: *Physica Status Solidi (A) Applied Research* 198.1 (2003), pp. 99–110.

[21] C. Mannequin, T. Tsuruoka, T. Hasegawa, and M. Aono. "Identification and roles of nonstoichiometric oxygen in amorphous Ta2O5thin films deposited by electron beam and sputtering processes." In: *Applied Surface Science* 385 (2016), pp. 426–435.

[22] C. Mannequin, T. Tsuruoka, T. Hasegawa, and M. Aono. "Identification and roles of nonstoichiometric oxygen in amorphous Ta2O5thin films deposited by electron beam and sputtering processes." In: *Applied Surface Science* 385 (2016), pp. 426–435.

[23] E. Nolot, B. Caby, R. Gassilloud, M. Veillerot, and D. Eichert. "X-ray reflectometry and grazing-incidence X-ray fluorescence characterization of innovative electrodes for tantalum-based resistive random access memories." In: *Spectrochimica Acta - Part B Atomic Spectroscopy* 149 (2018), pp. 71–75.

[24] P. Barquinha, L. Pereira, G. Goncalves, D. Kuscer, M. Kosec, A. Vila, A. Olziersky, J. R. Morante, R. Martins, and E. Fortunato. "Low-temperature sputtered mixtures of high-k and high bandgap dielectrics for GIZO TFTs." In: *Journal of the Society for Information Display* 18.10 (2010), p. 762.

[25] M Cevro. "Ion-beam sputtering of (Ta2O5)x - (SiO2)1 - x composite thin films." In: *Thin Solid Films* 258 (1995), pp. 91–103.

[26] P. Barquinha. "Transparent Oxide Thin-Film Transistors: production, characterization and integration." Ph.D. thesis. Nova University of Lisbon, 2010.

[27] R. Prachachet, P. Buranasiri, M. Horprathum, P. Eiamchai, S. Limwichean, V. Patthanasettakul, N. Nuntawong, P. Chindaudom, B. Samransuksamer, and T. Lertvanithphol. “Investigation of optical characteristics of the evaporated Ta2O5 thin films based on ellipsometry and spectroscopy.” In: *Materials Today: Proceedings*. Vol. 4. 5. 2017, pp. 6365–6371.

[28] S. Ezhilvalavan and T.-Y. Tseng. “Electrical properties of Ta2O5 thin films deposited on Ta.” In: *Applied Physics Letters* 74.17 (1999), p. 2477.

[29] R Waser and M Aono. “Nonoionics-based resistive switching memories.” In: *Nature Materials* 6 (2007), p. 833.

[30] D. Bhattacharyya, N. K. Sahoo, S. Thakur, and N. C. Das. “Spectroscopic ellipsometry of TiO2 layers prepared by ion-assisted electron-beam evaporation.” In: *Thin Solid Films* 360.1-2 (2000), pp. 96–102.

[31] J. Y. Zhang, I. W. Boyd, B. J. O’Sullivan, P. K. Hurley, P. V. Kelly, and J. P. Sénateur. “Nanocrystalline TiO2 films studied by optical, XRD and FTIR spectroscopy.” In: *Journal of Non-Crystalline Solids* 303.1 (2002), pp. 134–138.

[32] T. Tsuruoka, I. Valov, S. Tappertzhofen, J. Van Den Hurk, T. Hasegawa, R. Waser, and M. Aono. “Redox Reactions at Cu,Ag/Ta2O5 Interfaces and the Effects of Ta2O5 Film Density on the Forming Process in Atomic Switch Structures.” In: *Advanced Functional Materials* 25.40 (2015), pp. 6374–6381.

[33] A. P. P. Correia, P. M. Cândido Barquinha, and J. C.d. P. Goes. *A Second-Order ΣΔ ADC Using Sputtered IGZO TFTs*. Springer, 2016.

[34] C. Fernandes, A. Santa, Â. Santos, P. Bahubalindruni, J. Deuermeier, R. Martins, E. Fortunato, and P. Barquinha. “A Sustainable Approach to Flexible Electronics with Zinc-Tin Oxide Thin-Film Transistors.” In: *Advanced Electronic Materials* 1800032 (2018), p. 1800032.

[35] Y. Kuo. *Thin Film Transistors*. Ed. by Y. Kuo. Springer US, 2004.

[36] K. Nomura, H. Ohta, A. Takagi, T. Kamiya, M. Hirano, and H. Hosono. “Room-temperature fabrication of transparent flexible thin-film transistors using amorphous oxide semiconductors.” In: *Nature* 432.7016 (2004), pp. 488–492.

[37] European Commission. *Report on Critical Raw Materials and the Circular Economy*. 2018.

[38] D. H. Cho, S. Yang, C. Byun, J. Shin, M. K. Ryu, S. H. K. Park, C. S. Hwang, S. M. Chung, W. S. Cheong, S. M. Yoon, and H. Y. Chu. “Transparent Al-Zn-Sn-O thin film transistors prepared at low temperature.” In: *Applied Physics Letters* 93.14 (2008), p. 142111.

[39] D. L. Young, D. L. Williamson, and T. J. Coutts. “Structural characterization of zinc stannate thin films.” In: *Journal of Applied Physics* 91.3 (2002), pp. 1464–1471.

[40] E. M. C. Fortunato, L. M. N. Pereira, P. M. C. Barquinha, A. M. Botelho do Rego, G. Gonçalves, A. Vilà, J. R. Morante, and R. F. P. Martins. "High mobility indium free amorphous oxide thin film transistors." In: *Applied Physics Letters* 92.22 (2008), p. 222103.

[41] N. L. Dehuff, E. S. Kettenring, D. Hong, H. Q. Chiang, J. F. Wager, R. L. Hoffman, C. H. Park, and D. A. Keszler. "Transparent thin-film transistors with zinc indium oxide channel layer." In: *Journal of Applied Physics* 97.6 (2005), p. 064505.

[42] D. S. Han, Y. J. Kang, J. H. Park, H. T. Jeon, and J. W. Park. "Influence of molybdenum source/drain electrode contact resistance in amorphous zinc-tin-oxide (a-ZTO) thin film transistors." In: *Materials Research Bulletin* 58 (2014), pp. 174–177.

[43] N. P. Barradas, C. Jeynes, and R. P. Webb. "Simulated annealing analysis of Rutherford backscattering data." In: *Applied Physics Letters* 71.2 (1997), pp. 291–293.

[44] K. Hasche, P. Thomsen-schmidta, M. Krumreya, G. Adea, G. Virna, J. Stuempela, S. Schaedlichb, W. Frankc, M. Procopd, V. Beckd, D Braunschweig, and V. D. Eichen. "Metrological characterization of nanometer film thickness standards for XRR and ellipsometry applications." In: *Spie* 5190.2003 (2003), pp. 165–172.

[45] S. Kohli, C. D. Rithner, P. K. Dorhout, A. M. Dummer, and C. S. Menoni. "Comparison of nanometer-thick films by x-ray reflectivity and spectroscopic ellipsometry." In: *Review of Scientific Instruments* 76.2 (2005), pp. 10–15.

[46] M. F. Toney, C. M. Mate, K. A. Leach, and D. Pocker. "Thickness measurements of thin perfluoropolyether polymer films on silicon and amorphous-hydrogenated carbon with X-ray reflectivity, ESCA and optical ellipsometry." In: *Journal of Colloid and Interface Science* 225.1 (2000), pp. 219–226.

[47] H. Águas, V. Silva, E. Fortunato, S. Lebib, P. Roca i Cabarrocas, I. Ferreira, L. Guimarães, and R. Martins. "Large Area Deposition of Polymorphous Silicon by Plasma Enhanced Chemical Vapor Deposition at 27.12 MHz and 13.56 MHz." In: *Japanese Journal of Applied Physics, Part 1: Regular Papers and Short Notes and Review Papers* 42.8 (2003), pp. 4935–4942.

[48] J. Capilla, J. Olivares, M. Clement, J. Sangrador, E. Iborra, and A. Devos. "Characterization of amorphous tantalum oxide for insulating acoustic mirrors." In: *Proceedings of the IEEE International Frequency Control Symposium and Exposition*. IEEE, 2011, pp. 1–6.

[49] T. Iroh. *Beam Modification of Materials*. 1st editio. Vol. 1. Amsterdam: Elsevier, 1989, p. ii.

[50] F. Giustino, P. Umari, and A. Pasquarello. "Dielectric effect of a thin SiO2 interlayer at the interface between silicon and high-k oxides." In: *Microelectronic Engineering*. Vol. 72. 1-4. 2004, pp. 299–303.

[51] J. Robertson. "High dielectric constant oxides." In: *The European Physical Journal Applied Physics* 28.3 (2004), pp. 265–291.

[52] T. Busani and R. A. Devine. "The importance of network structure in high-k dielectrics: LaAlO3, Pr2O3, and Ta2O5." In: *Journal of Applied Physics* 98.4 (2005), p. 044102.

[53] L. Névot and P. Croce. "Caractérisation des surfaces par réflexion rasante de rayons X. Application à l'étude du polissage de quelques verres silicates." In: *Revue de Physique Appliquée* 15.3 (1980), pp. 761–779.

Appendix A

Abelès matrix formalism

In order to extract the properties of the films out of the data obtained by XRR, the analyses were performed in the *MOTOFIT 4.1* package [4]. This package works within *IGOR* (Wavematrics) and uses the Abelès matrix formalism. In this formalism, the reflectivity is calculated as a function of the momentum transfer (Q):

$$Q = \frac{4\pi}{\lambda} sin(\theta) = 2k_z \tag{A.1}$$

where λ is the wavelength of the incident radiation, θ is the angle of the incident radiation and k_z the wave factor. The SLD profile is what makes the measured reflectivity vary and it is normally changing as a depth function. Despite that, a good approximation can be done if one considers the samples as a group of layers with determined thickness, roughness and SLD (which is a function that depends on the mass density and the composition of the layers).

In the Abelès matrix formalism the obtained reflectivity is calculated from the multiplication of the characteristic matrix of each layer. To calculate this matrix, three variables are needed: the wave factor (that is a function of the SLD), the layer thickness and the Fresnel reflection coefficient. The Fresnel reflection coefficient between two layers is given by:

$$r_{n,n+1} = \frac{k_n - k_{n+1}}{k_n + k_{n+1}} \tag{A.2}$$

This does not takes into account the roughness/diffuseness of the layer. So, it is used a Fresnel reflection coefficient with an error function [53]:

$$r_{n,n+1} = \frac{k_n - k_{n+1}}{k_n + k_{n+1}} (-2k_n^2 + \sigma_{n,n+1}^2) \tag{A.3}$$

where $\sigma_{n,n+1}$ is the roughness/diffuseness [4].

Tutorial of XRR data analysis in *MOTOFIT*

This tutorial assumes that the data analysis will be performed in the computer used at CENIMAT to analyse XRR and X-ray diffraction data. On that computer *IGOR*, *MOTOFIT* and *Python* with the respective packages have already been installed. This tutorial is based in the experience acquired during the present work and in the *MOTOFIT* manual that can be found at http://motofit.sourceforge.net/manual/motofit/motofitmanual.pdf that was written by Andrew Nelson. In the manual you can find more detailed information about *MOTOFIT*.

In the beginning you must have a *.csv* file generated by the PANalytical's X'Pert PRO MRD X-ray diffractometer in the CENIMAT. These files contain the information of the characterization as well as the measured data (detected intensity as a function of the angle of incidence). In order to use the *MOTOFIT* package the data must be converted to obtained the normalised intensity as a function of the photon momentum.

To convert the data you must use the *Python* function *data_converter_Motofit.py*. After opening the function a file selection dialog box appears. There you must select all files you want to convert. After the conversion new files will appear in the same folder in which the original files are stored. If the original file name is *example.csv*, the converted file name will be *example_motofit.csv*.

In order to open the *MOTOFIT* package, you have to open *IGOR* and go to *Motofit* > *Fit Reflectivity data* > *Continue*. In the *Reflectivity panel* it is possible to find four menu tabs and in the *Fit* tab it is possible to find four menu boxes (Figure B.1).

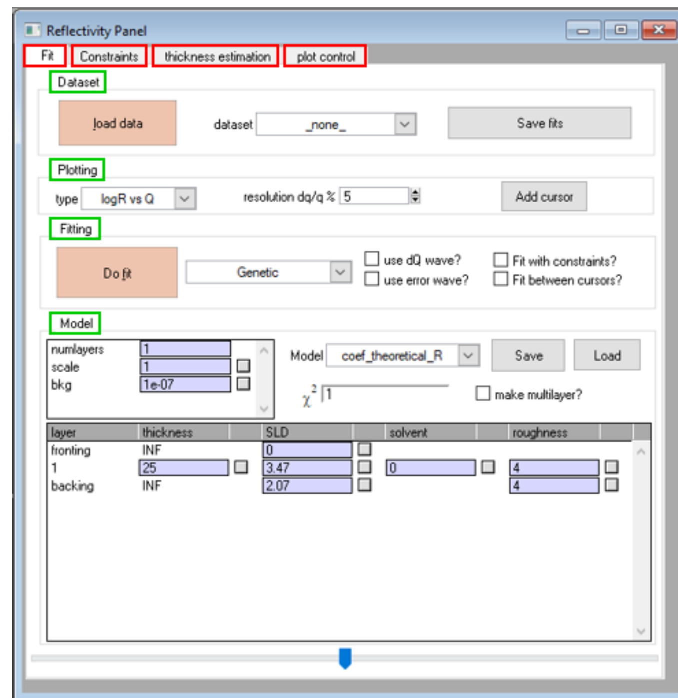

Figure B.1: Reflectivity panel of *MOTOFIT* with the menu taps in the red boxes and the menu boxes in the green boxes.

In the *Dataset* menu box, by clicking in *load data* you can choose the file to be analysed. Beware of two points: choose the *_motofit.csv* files (the converted files) and confirm that you are working in the right file. After loading one file, if you load a second one the program will continue to work in the first file by default. You can confirm and choose the right file to work in *data set*.

In the *Model* menu box you can load a file with the coefficients if you already have it. If not you can define all the parameters. All the parameters that you are certain about you should set them as fixed. An example is presented in Figure B.2. In this case it is a sample of Ta_2O_5 film in a silicon wafer. For a silicon wafer the *backing* has a fixed value for the SLD as 20.124×10^{-6} Å^{-2}. The *layer 2* is the native silicon oxide, so the SLD value was fixed in 18.886×10^{-6} Å^{-2}. The third layer is the Ta_2O_5. These SLD values were obtained using the *SLD calculator* in the *Motofit* tab.

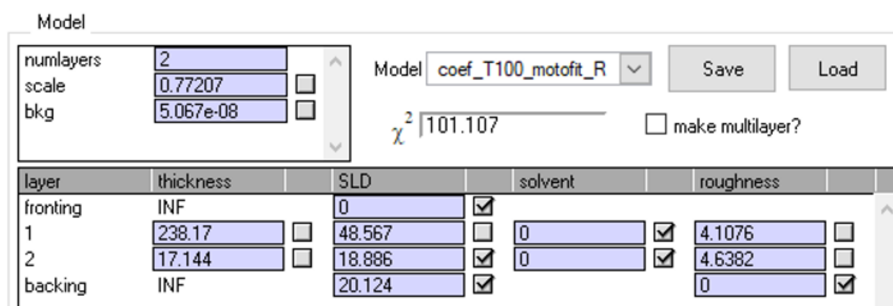

Figure B.2: An example of a model with fixed parameters.

In the *Fitting* menu box you can perform the fit by clicking in *Do fit*. A first fit should be done with the *Genetic* option selected. This is the best way to have a better idea of the parameters. Then the *Gencurvefit limits* windows will appear. Here you must define the limits for the parameters' fitting. The number of iterations and the population size of the fit can be higher if necessary. After clicking in *Do fit* the results will be shown. It may be necessary to adjust the *resolution dq/q %* in the *Plotting* menu box.

Once you already have a good idea of the parameters you should perform a fitting with the *Genetic + LM* option selected. This performs a genetic optimization and uses the Levenberg-Maquardt algorithm to have more accurate results and the respective uncertainties. You must be aware that if the defined limits of the parameters' fitting are too vague, the fit may not present viable results. This is the reason why the genetic fitting must be done in the first place. The final results will be the SLD profile in the *Scattering lengh density* window (Figure B.3) and the parameters with the respective uncertainty in the window below (Figure B.4). To export the fitted graphic, you can use the *Save fits* in the *Dataset* box menu. You must choose the option with the same name as the file.

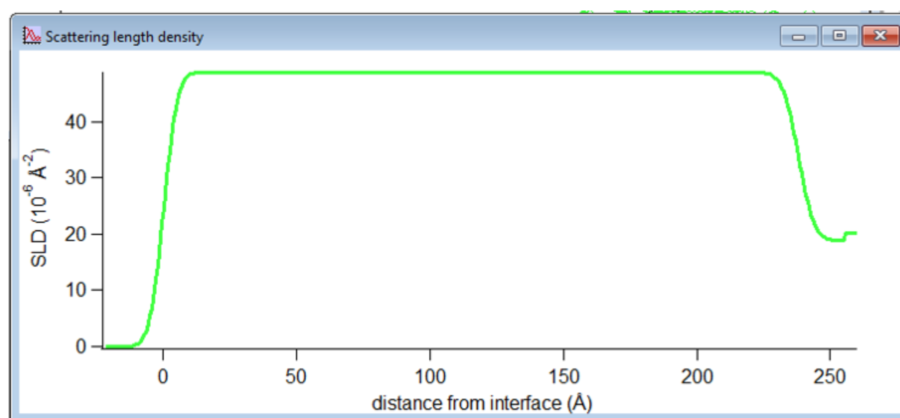

Figure B.3: Results of the SLD profile of the sample.

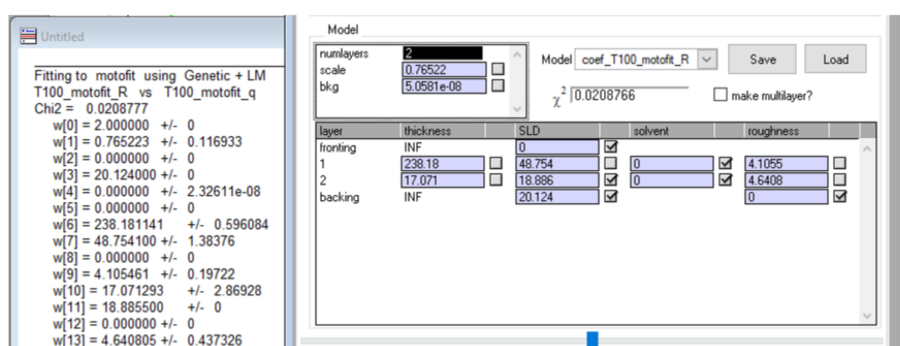

Figure B.4: Results of the parameters of the sample with the respective uncertainties.

If you are sure that some parameters are correlated, you can use that information in the *Constraints* tab menu. As an example, if that information is «the SLD of the layer 1 is equal do the SLD of layer 2», the input will be *K7=K15*. The explanation of the number of the parameters is shown in Figure B.5.

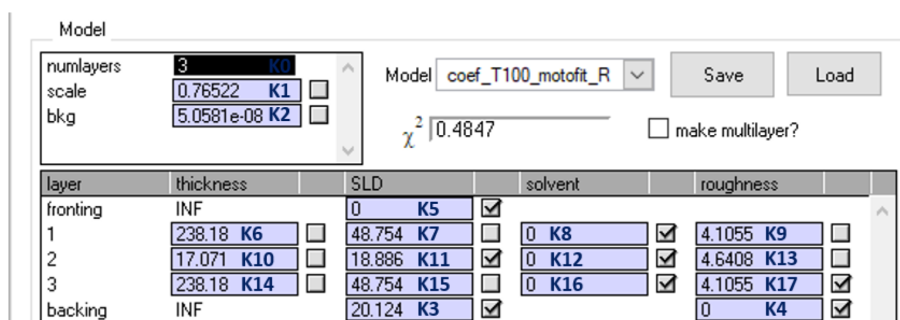

Figure B.5: Results of the parameters of the sample with the respective uncertainties.

The *plot control* tab menu can be used to define which lines can or cannot be shown. By clicking twice in the lines of the graphic you can modify them.

One final remark must be done: every time you use *MOTOFIT* to get information to include in a publication you have to give credits to the author citing the paper:

A. Nelson. "Co-refinement of multiple-contrast neutron/X-ray reflectivity data using MOTOFIT." In: *Journal of Applied Crystallography* 39.2 (2006), pp. 273–276.

Appendix C

Error functions of the performed fits

Table C.1: χ^2 of the fits performed in the Ta_2O_5 samples (section 3.1).

Sample	XRR	SE
Si wafer	0.0178582	0.373754
Ta1	0.00613824	0.175486
Ta2	0.0150852	4.190142
Ta3	0.00780566	1.683170
Ta4	0.0208817	3.329095
Ta5	0.0284124	3.497609
Ta6	0.0267322	5.451688

Table C.2: χ^2 of the fits performed in the TaSiO samples (section 3.2).

Sample	gr-TaSi			d-TaSi		Table 3.10
	XRR	SE	RBS	SE	RBS	SE
Ta1Si	0.0158015	0.195114	60.67	-		-
Ta2Si	0.055409	1.524357	30.9	7.187333		7.353949
Ta3Si	0.017355	0.973171	8.2	4.365729		4.574820
Ta4Si	0.012244	1.868353	7.2	4.143032		4.395866
Ta5Si	0.0233148	1.222181	8.0	5.474410		5.877838
Ta6Si	0.0148769	1.136910	11.9	6.183555		7.297378
Ta4	0.0249664	2.261642	8.525	7.525571		7.513732

Table C.3: χ^2 of the fits performed in the ZTO samples (section 3.3).

Sample	XRR	SE
P1-O2-H1	0.0364218	1.288003
P1-O2-H2	0.0605636	1.142378
P1-O2-H3	0.0490492	1.177760
P2-O1-H1	0.0428692	0.545678
P2-O2-H1	0.0188471	0.510383
P2-O2-H2	0.0211289	0.732384
P2-O2-H3	0.0237625	0.579150
P2-O3-H1	0.0637746	0.567632
P2-O3-H2	0.0546619	0.413325
P2-O3-H3	0.0481622	0.393520

Appendix D

Python fuction to convert data to be used in *MOTOFIT*

```python
# -*- coding: utf-8 -*-
"""
Created on Mon Apr 30 09:16:58 2018

@author: Tiago Gonçalves
"""
#This program converts files from XRR analysis from CENIMAT's diffractometer
#into data that can be analysed by Motofit

import numpy as np
from tkinter import filedialog
from tkinter import *

#To select the files:
root = Tk()
root.withdraw()
files_path = filedialog.askopenfilenames(filetypes = (("CSV files","*.csv"),
                                                      ("all files","*.*")))
number_files = len(files_path)
z = 0

#Runs through all files
while z < number_files:
    data = np.genfromtxt(files_path[z], delimiter = ',', skip_header = 29)
    length = len(data)
    max_intensity = np.max(data)
    i = 0
    #Converts the values
    while i < length:
        data[i , 0] = 4 * np.pi * np.sin(np.radians(data[i , 0])) / 1.5405980
        data[i , 1] /= max_intensity
        i += 1
    #Save the new files
    np.savetxt(files_path[z][:-4] + '_motofit.csv', data,
               fmt = '%.9f,%.25f')
    z += 1
```

Appendix E

Complementary schemes

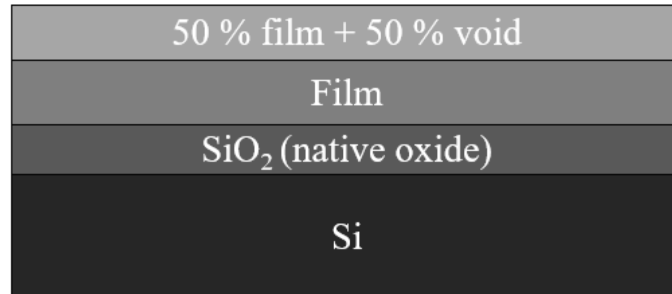

Figure E.1: Model used to perform the fit of the data obtained by SE.

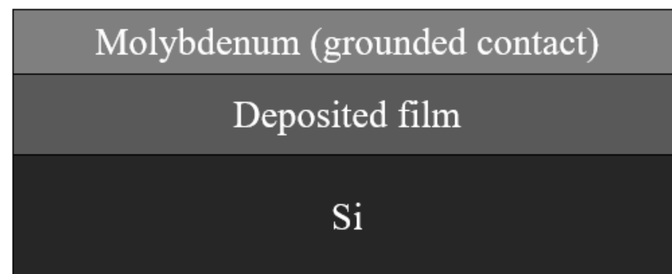

Figure E.2: Scheme of the MIS structure.

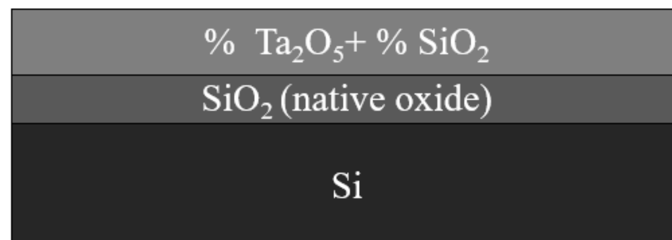

Figure E.3: Model used to perform the fit of the data obtained by SE to get the composition of the films.

Appendix F

Analysis of a silicon wafer

For the characterization of the Ta_2O_5 films a piece of the silicon wafer where all films were grown was previously characterized. Here the objective was to lower the number of the fitting parameters of the XRR and the SE data analysis. More specifically one aimed to get the thickness and roughness of the native oxide and the SLD of both the native oxide and the Si, so these parameters could be used as fixed values for all samples.

Despite the attempts, one had to use the theoretical values of the SLD to get reliable fits in the XRR data analysis. Those values were obtained in the *SLD calculator* of *MOTOFIT*. The reason for this problem is the similarity of Si and SiO_2 electron densities [45].

K. Hasche *et al.* [44] were able to find a good contrast between the SLD of Si and SiO_2, which lead them to achieve thicknesses with low uncertainties. This was due to the photon energy of 1841 eV used because, at this photon energy, the Si extinction coefficient has a local maximum while the SiO_2 extinction coefficient remains low.

In this work, the fitting of those parameters revealed to be impracticable. When fitted the obtained results were physically incorrect or both values of SLD were identical when one considered the uncertainty of those values. So, the SLD of Si and SiO_2 used were 18.886×10^{-6} and 20.124×10^{-6} Å^{-2} respectively.

Besides the problem with the SLD, the roughness of the native oxide could not be fitted in the SE data analysis. Here the roughness is represented by the thickness of a layer where the components are 50 % of void and 50 % of the native oxide. When the thickness of this layer was fitted, the result was 0.1 Å which is the limit of the software, so it is meaningless.

Nevertheless, as one can see in Table F.1, the SiO_2 thickness obtained by SE has a very low uncertainty. Because of that, for the SE data analysis of the Ta_2O_5 samples, 20.0 Å was the fixed value of the SiO_2 thickness used. However, the same did not happen with the XRR results. The uncertainty associated with SiO_2 thickness is about 11 % of its value so the SiO_2 thickness remained a fitting parameter in the XRR analysis. Despite that it is important to see that, given the associated uncertainties, both techniques are in agreement.

Table F.1: Results of XRR and SE analyses of a silicon wafer using Si and SiO_2 SLD values of 18.886×10^{-6} and 20.124×10^{-6} Å^{-2}, respectively.

Technique	SiO_2	
	Thickness (Å)	Roughness (Å)
SE	20.0 ± 0.3	-
XRR	18 ± 2	5.2 ± 0.3

One important remark about the silicon wafer XRR analysis, as it is possible to see in Figure F.1, is the fact that the fitting does not present the SiO_2 Kiessing fringes as it should. Nevertheless, the results obtained above (Table F.1) were the expected ones. This can be caused by a possible limitation of the software used.

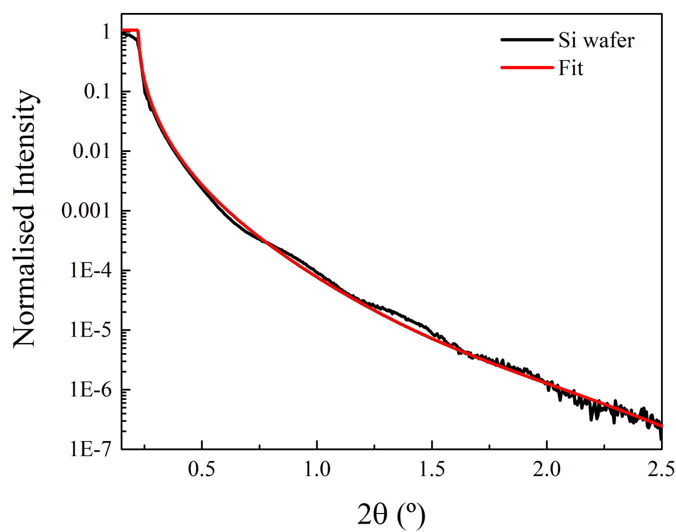

Figure F.1: Real data and XRR fit of the silicon wafer.

RBS analysis

In this Appendix the analysis of the RBS measured data of a single sample will be presented as an example. The data analysis procedure was the same for all samples.

In RBS a beam of ions is directed onto the sample to be measured. A He^+ beam was used in the present work. The number and the energy of the backscattered ions are measured. On one hand the number of backscattered ions with a specific energy is proportional to the concentration of the element of that respective energy. On the other hand the energy of each backscattered ion depends on two factors: the mass of the atom in which it was scattered and the depth of that atom in the sample.

In Figure G.1 the energy barriers are indicated for each element present in the sample. The Ar was also included since its presence is predicted due to its usage in the rf sputtering process. To perform the fit one assumed that the sample was made of Ta_2O_5 and SiO_2 besides Ar. The fit could have been done with the individual elements instead of the molecules but the quantification of O is very difficult and uncertain.

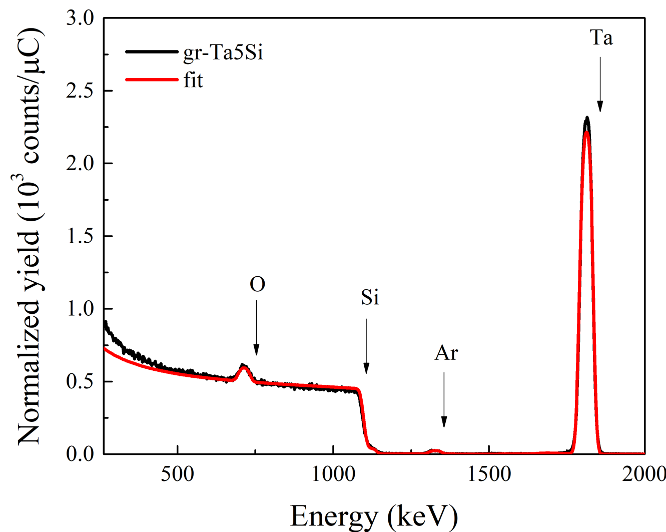

Figure G.1: Fit and treated data measured by RBS from the gr-Ta5Si sample.

From the fitting it is possible to get the information presented in Table G.1. The units of the obtained thickness are atoms cm^{-2}, but to compare with the other techniques it is necessary to convert to Å.

Table G.1: Results from the performed fit of the gr-Ta5Si sample.

Thickness (10^{15} atoms cm^{-2})	Ta_2O_5 (molecular %)	SiO_2 (molecular %)	Ar (molecular %)
377.5	70.1	25.5	3.3

To do the conversion it is necessary to use the composition of the film, the mass density and molecular mass of each component. The problem is that Ar is a gas which means that it does not have a mass density value. To solve this problem an approximation was done: the Ar was not considered and the normalized composition was used. In other words, the assumed composition was 73.3 molecular % of Ta_2O_5 and 26.7 molecular % of SiO_2. The mass densities used for the Ta_2O_5 and SiO_2 were 8.2 and 2.2 $g\,cm^{-3}$, respectively [48].

The first step is to get a density in atoms cm^{-3} for each component. Here one uses the mass density, molecular mass and the Avogadro constant. Then, dividing the RBS thickness by the weighted density (taking into account the normalized composition) one gets the thickness in a length unit (in this case cm).

Appendix H

Parameters of the Tauc-Lorentz models obtained by spectroscopic ellipsometry

Table H.1: Parameters from a Tauc-Lorentz oscillator of Ta_2O_5 samples (section 3.1).

Sample	E_g (eV)	ε_∞	A (eV)	E (eV)	C (eV)
Ta1	3.6 ± 0.2	3.2 ± 0.2	81 ± 17	5.3 ± 0.2	2.6 ± 0.2
Ta2	4.31 ± 0.03	2.5 ± 0.2	276 ± 20	5.08 ± 0.04	1.77 ± 0.04
Ta3	4.31 ± 0.02	2.12 ± 0.05	323 ± 10	4.97 ± 0.03	1.84 ± 0.03
Ta4	4.28 ± 0.02	2.42 ± 0.08	278 ± 11	5.06 ± 0.03	1.81 ± 0.03
Ta5	4.20 ± 0.02	2.14 ± 0.05	264 ± 15	5.09 ± 0.04	2.02 ± 0.03
Ta6	4.23 ± 0.02	2.21 ± 0.06	264 ± 12	5.10 ± 0.04	1.92 ± 0.03

Table H.2: Parameters from a double Tauc-Lorentz oscillator of TaSiO samples used to determine the grow rate (section 3.2.1).

Sample	E_g (eV)	ε_∞	$A1$ (eV)	$E1$ (eV)	$C1$ (eV)	$A2$ (eV)	$E2$ (eV)	$C2$ (eV)
gr-Ta1Si	-1.8 ± 0.5	-46 ± 10	494 ± 75	7.38 ± 0.04	1.84 ± 0.06	112 ± 17	4.37 ± 0.02	0.55 ± 0.4
gr-Ta2Si	4.773 ± 0.007	0.8 ± 0.3	42 ± 10	24 ± 4	1.0 ± 0.4	353 ± 10	4.40 ± 0.03	2.46 ± 0.03
gr-Ta3Si	4.47 ± 0.02	0.4 ± 0.2	69 ± 5	10.4 ± 0.3	0.02 ± 0.097	90 ± 4	5.58 ± 0.02	1.78 ± 0.03
gr-Ta4Si	4.30 ± 0.02	1.9 ± 0.1	24 ± 2	8.0 ± 0.4	2.6 ± 0.4	132 ± 6	5.44 ± 0.02	1.89 ± 0.03
gr-Ta5Si	4.20 ± 0.02	1.0 ± 0.2	64 ± 7	10.2 ± 0.6	7.8 ± 0.6	116 ± 4	5.48 ± 0.02	1.70 ± 0.03
gr-Ta6Si	4.18 ± 0.02	1.48 ± 0.07	77 ± 9	7.1 ± 0.3	5.6 ± 0.4	87 ± 5	5.45 ± 0.02	1.49 ± 0.05
gr-Ta4	4.09 ± 0.02	1.4 ± 0.2	83 ± 15	7.9 ± 0.9	9 ± 2	143 ± 9	5.27 ± 8.3	1.57 ± 0.04

Table H.3: Parameters from a double Tauc-Lorentz oscillator of TaSiO samples used as a dielectric material (section 3.2.2).

Sample	E_g (eV)	ε_∞	$A1$ (eV)	$E1$ (eV)	$C1$ (eV)	$A2$ (eV)	$E2$ (eV)	$C2$ (eV)
d-Ta2Si	4.53 ± 0.03	1.74 ± 0.06	54 ± 9	7.3 ± 0.4	4.0 ± 0.3	40 ± 5	5.65 ± 0.07	1.57 ± 0.08
d-Ta3Si	4.25 ± 0.02	1.96 ± 0.03	59 ± 4	6.71 ± 0.08	2.9 ± 0.2	40 ± 2	5.52 ± 0.02	1.11 ± 0.03
d-Ta4Si	4.237 ± 0.007	1.78 ± 0.03	65 ± 4	7.0 ± 0.2	4.1 ± 0.2	72 ± 3	5.48 ± 0.02	1.40 ± 0.03
d-Ta5Si	4.254 ± 0.008	1.79 ± 0.04	81 ± 7	6.5 ± 0.2	4.1 ± 0.2	77 ± 4	5.42 ± 0.02	1.42 ± 0.03
d-Ta6Si	4.19 ± 0.02	1.80 ± 0.04	96 ± 8	6.3 ± 0.2	4.0 ± 0.2	66 ± 4	5.39 ± 0.02	1.19 ± 0.03
d-Ta4	4.172 ± 0.008	1.8 ± 0.3	102 ± 10	6.6 ± 0.4	9.5 ± 0.6	161 ± 5	5.24 ± 0.02	1.59 ± 0.02

Table H.4: Parameters from a double Tauc-Lorentz oscillator of ZTO samples in the study of the influence of the rf power (section 3.3.1).

Sample	E_g (eV)	ε_∞	$A1$ (eV)	$E1$ (eV)	$C1$ (eV)	$A2$ (eV)	$E2$ (eV)	$C2$ (eV)
P1-H1-O2	2.85 ± 0.05	1.2 ± 0.5	94 ± 4	10.5 ± 0.6	15.6 ± 0.8	12 ± 2	4.49 ± 0.04	2.2 ± 0.2
P2-H1-O2	3.0 ± 0.1	1.0 ± 0.7	136 ± 13	13 ± 1	22 ± 2	19 ± 5	4.29 ± 0.08	1.7 ± 0.1
P1-H2-O2	3.00 ± 0.04	1.5 ± 0.4	91 ± 4	9.5 ± 0.5	14.3 ± 0.6	12 ± 2	4.51 ± 0.03	1.9 ± 0.1
P2-H2-O2	3.0 ± 0.1	0.9 ± 0.7	166 ± 21	16 ± 2	29 ± 3	24 ± 7	4.2 ± 0.1	2.0 ± 0.1
P1-H3-O2	2.96 ± 0.04	1.1 ± 0.5	93 ± 4	10.3 ± 0.6	15.1 ± 0.6	12 ± 2	4.54 ± 0.04	2.0 ± 0.2
P2-H3-O2	3.0 ± 0.1	0.4 ± 0.6	174 ± 17	16 ± 2	29 ± 3	21 ± 6	4.22 ± 0.09	1.9 ± 0.1

Table H.5: Parameters from a double Tauc-Lorentz oscillator of ZTO samples in the study of the influence of the H_2 flow (section 3.3.2).

Sample	E_g (eV)	ε_∞	*A1* (eV)	*E1* (eV)	*C1* (eV)	*A2* (eV)	*E2* (eV)	*C2* (eV)
P1-H1-O2	2.85 ± 0.05	1.2 ± 0.5	94 ± 4	10.5 ± 0.6	15.6 ± 0.8	12 ± 2	4.49 ± 0.04	2.2 ± 0.2
P1-H2-O2	3.00 ± 0.04	1.5 ± 0.4	91 ± 4	9.5 ± 0.5	14.3 ± 0.6	12 ± 2	4.51 ± 0.03	1.9 ± 0.1
P1-H3-O2	2.96 ± 0.04	1.1 ± 0.5	93 ± 4	10.3 ± 0.6	15.1 ± 0.6	12 ± 2	4.54 ± 0.04	2.0 ± 0.2
P2-H1-O2	3.0 ± 0.1	1.0 ± 0.7	136 ± 13	13 ± 1	22 ± 2	19 ± 5	4.29 ± 0.08	1.7 ± 0.1
P2-H2-O2	3.0 ± 0.1	0.9 ± 0.7	166 ± 21	16 ± 2	29 ± 3	24 ± 7	4.2 ± 0.1	2.0 ± 0.1
P2-H3-O2	3.0 ± 0.1	0.4 ± 0.6	174 ± 17	16 ± 2	29 ± 3	21 ± 6	4.22 ± 0.09	1.9 ± 0.1
P2-H1-O3	3.0 ± 0.1	0.5 ± 0.6	182 ± 22	16 ± 2	31 ± 4	16 ± 2	4.20 ± 0.09	1.92 ± 0.08
P2-H2-O3	3.01 ± 0.09	-0.5 ± 0.6	186 ± 17	16 ± 1	27 ± 3	25 ± 6	4.24 ± 0.08	1.98 ± 0.09
P2-H3-O3	3.0 ± 0.1	-0.1 ± 0.6	162 ± 16	15 ± 1	24 ± 3	22 ± 6	4.34 ± 0.08	1.9 ± 0.1

Table H.6: Parameters from a double Tauc-Lorentz oscillator of ZTO samples in the study of the influence of the O_2 flow (section 3.3.3).

Sample	E_g (eV)	ε_∞	*A1* (eV)	*E1* (eV)	*C1* (eV)	*A2* (eV)	*E2* (eV)	*C2* (eV)
P2-H1-O1	2.94 ± 0.08	1.6 ± 0.5	135 ± 14	14 ± 1	25 ± 2	29 ± 6	3.94 ± 0.09	2.1 ± 0.1
P2-H1-O2	3.0 ± 0.1	1.0 ± 0.7	136 ± 13	13 ± 1	22 ± 2	19 ± 5	4.29 ± 0.08	1.7 ± 0.1
P2-H1-O3	3.0 ± 0.1	0.5 ± 0.6	182 ± 22	16 ± 2	31 ± 4	16 ± 2	4.20 ± 0.09	1.92 ± 0.08
P2-H2-O2	3.0 ± 0.1	0.9 ± 0.7	166 ± 21	16 ± 2	29 ± 3	24 ± 7	4.2 ± 0.1	2.0 ± 0.1
P2-H2-O3	3.01 ± 0.09	-0.5 ± 0.6	186 ± 17	16 ± 1	27 ± 3	25 ± 6	4.24 ± 0.08	1.98 ± 0.09
P2-H3-O2	3.0 ± 0.1	0.4 ± 0.6	174 ± 17	16 ± 2	29 ± 3	21 ± 6	4.22 ± 0.09	1.9 ± 0.1
P2-H3-O3	3.0 ± 0.1	-0.1 ± 0.6	162 ± 16	15 ± 1	24 ± 3	22 ± 6	4.34 ± 0.08	1.9 ± 0.1

The real and imaginary part of the dielectric function of the ZTO samples

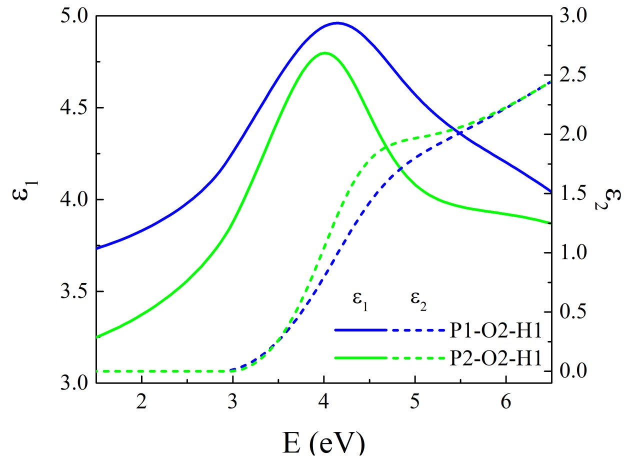

(a)

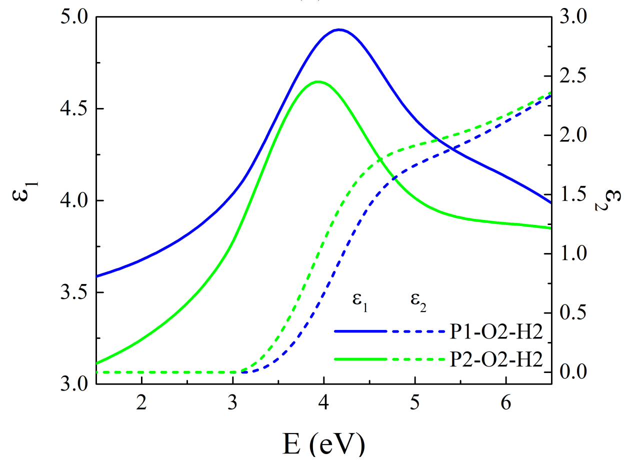

(b)

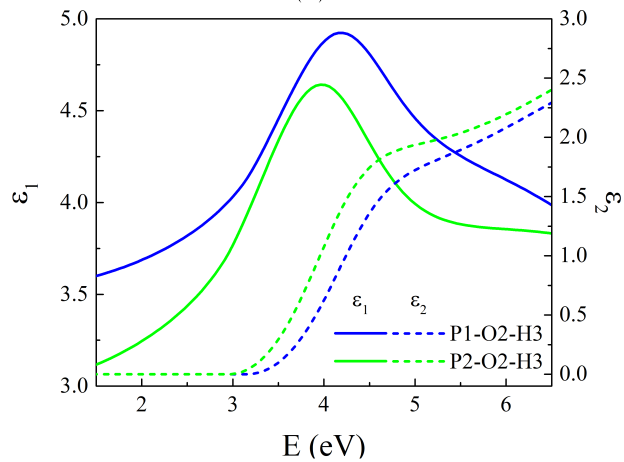

(c)

Figure I.1: Real and imaginary part of the dielectric function of the samples characterized in section 3.3.1.

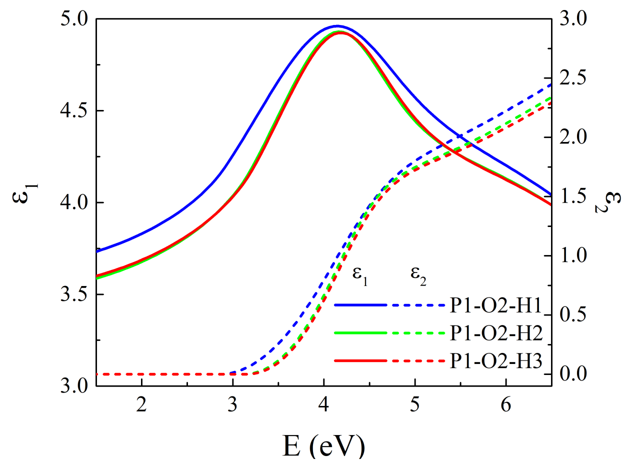

(a)

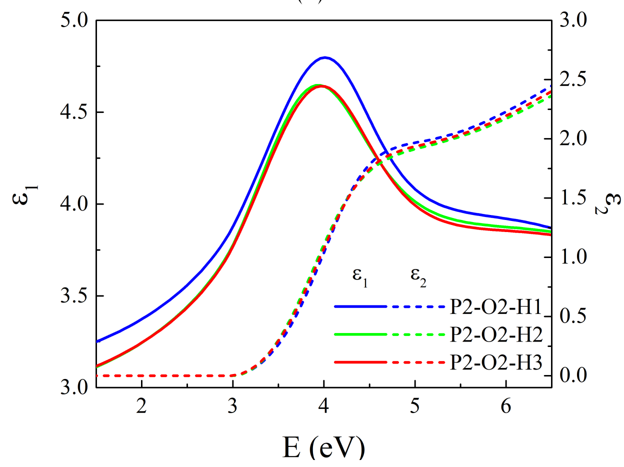

(b)

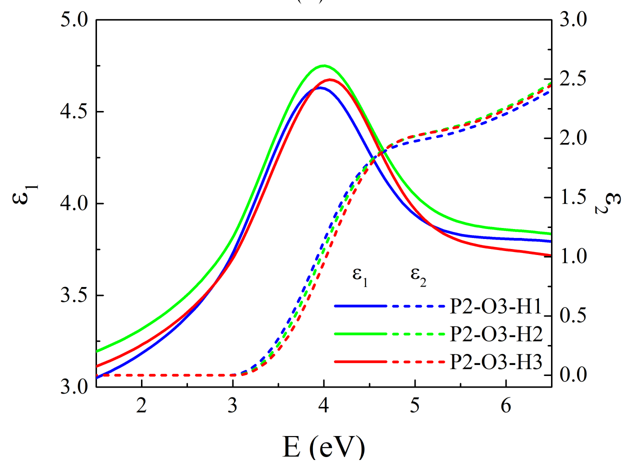

(c)

Figure I.2: Real and imaginary part of the dielectric function of the samples characterized in section 3.3.2.

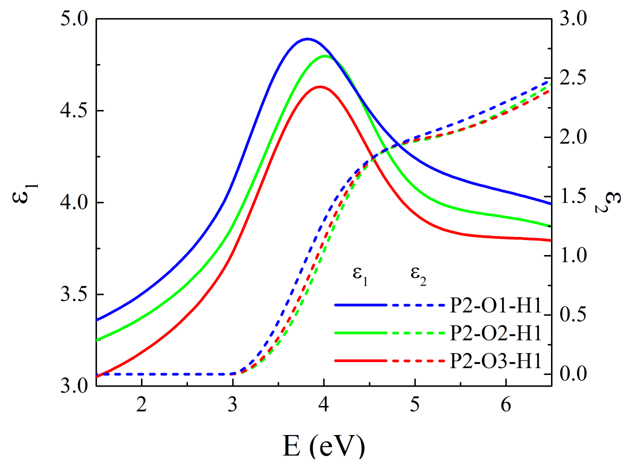

(a)

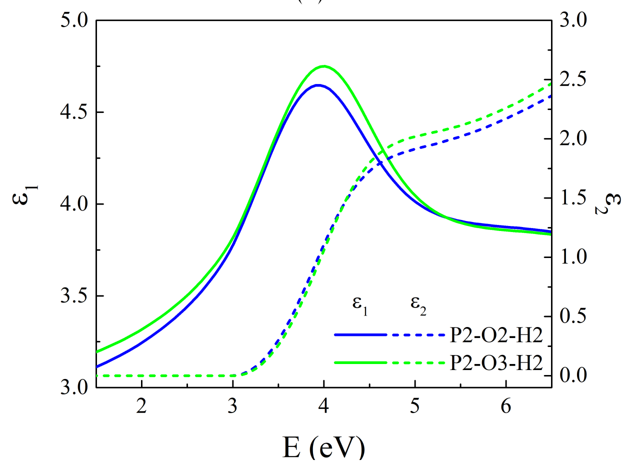

(b)

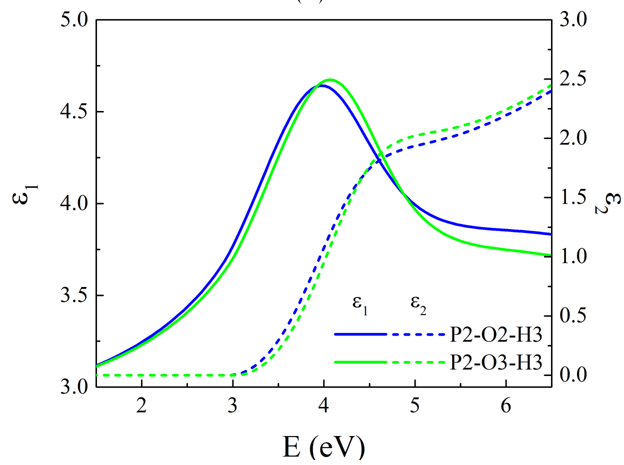

(c)

Figure I.3: Real and imaginary part of the dielectric function of the samples characterized in section 3.3.3.